BRD2 Upregulation as a Pan-Cancer Adaptive Resistance Mechanism to BET Inhibition

Suyakarn Archasappawat[1,2], Juliette Jacques[1], EunJung Lee[1], and Chang-il Hwang[1,2]

[1] Department of Microbiology and Molecular Genetics, College of Biological Sciences, University of California, Davis, CA

[2] University of California Davis Comprehensive Cancer Center, Sacramento, CA

Corresponding author: cihwang@ucdavis.edu

ABSTRACT

Bromodomain and extraterminal motif (BET) inhibitors, such as JQ1, are promising cancer therapeutics that target epigenetic regulators, particularly BRD4. However, resistance to BET inhibitors (BETi) limits their clinical utility, necessitating a better understanding of adaptive mechanisms. We identified BRD2 upregulation as a conserved response to BET inhibition across multiple cancer types and hypothesized that BRD2 compensates for BRD4 loss, sustaining essential transcriptional programs upon treatment. Consistent with this, BRD2 knockdown sensitized cancer cells to BETi *in vitro*, and combining BRD2 depletion and JQ1 treatment significantly impaired tumor growth *in vivo*. At the chromatin level, BRD2 and BRD4 ChIP-seq analysis of pancreatic cancer cells showed consistent BRD4 loss from chromatin after JQ1 treatment, while BRD2 displacement differed by sensitivity. Resistant cells maintained higher BRD2 occupancy than sensitive cells, suggesting a link between BRD2 retention and drug response. Mechanistically, NFYA mediates BRD2 up-regulation as NFYA depletion abrogated BRD2 upregulation upon BETi treatment. Collectively, our findings establish BRD2 as a critical mediator of adaptive resistance to BETi in pan-cancer and identify NFYA as a novel transcriptional regulator of this process. Co-targeting BRD2 or its regulatory network offers a rational strategy to enhance the durability and efficacy of BET-based therapies.

INTRODUCTION

Cancer progression can be driven by epigenetic reprogramming, which has recently been recognized as a fundamental hallmark of cancer (1,2). Epigenetic alterations enable cancer cells to activate oncogenic programs, silence tumor suppressors and adapt to microenvironmental stress, thereby promoting cancer progression and metastasis (3). Importantly, while conferring plasticity and survival, these changes render cancer cells dependent on aberrant epigenetic regulation to sustain malignant phenotype —vulnerabilities that can be therapeutically exploited. Central to this process is the molecular machinery that regulates epigenetic states, coordinated by three major classes of proteins: writers, readers and erasers. Writers deposit modifications such as DNA methylation or histone acetylation, erasers remove them, and readers interpret these marks to regulate downstream transcriptional activity. Together, these mechanisms dynamically shape transcriptional programs, often hijacked during carcinogenesis.

Among these regulators, the BET (bromodomain and extra-terminal domain) family has drawn significant attention as a group of critical epigenetic readers. This family comprises four members—BRD2, BRD3, BRD4, and the testis-specific BRDT—all sharing a key structural feature: two tandem N-terminal bromodomains that recognize and bind acetylated lysine residues on histones to anchor transcriptional machinery at active chromatin (4,5). Of these, BRD4 is the most extensively studied and plays a critical role at enhancer and super-enhancers (SEs), large regulatory clusters that drive the expression of key oncogenes, such as MYC (6). In addition to tethering to acetylated chromatin, BRD4 also recruits and scaffolds the Mediator complex and the P-TEFb kinase to release paused RNA polymerase II, thereby sustaining high-level transcription of target genes (7). Collectively, the actions of BRD4 support self-reinforcing transcriptional programs driven by short-lived oncogenic MYC transcripts (3). Because direct pharmacologic inhibition of MYC has proven difficult, BRD4 represents an attractive therapeutic vulnerability. Small-molecule BET inhibitors (BETi) such as JQ1 competitively bind to the bromodomains—

most potently of BRD4—displacing them from chromatin and dismantling SE–driven transcription (8). This results in rapid MYC downregulation and potent antitumor effects in preclinical models, with notable success in MYC-addicted hematologic malignancies and increasing exploration across diverse cancer types (9-11).

Despite these promising preclinical outcomes, clinical responses to BETi have been modest and short-lived, with resistance posing as a major barrier for translation (12-14). To date, most mechanistic insights into BETi resistance have come from models of acquired resistance following prolonged drug exposure, in which cancer cells undergo extensive transcriptional and epigenetic rewiring. Such models may not reflect the clinically relevant dynamics of adaptive resistance, defined by early and reversible changes that enable cancer cells to tolerate BET inhibition. A deeper understanding of the early adaptive responses to BET inhibition could reveal vulnerabilities that precede the emergence of acquired resistance and guide the development of more effective upfront or combination therapies.

In this study, we uncovered upregulation of BRD2—a BRD4 paralog—as an adaptive response to BET inhibition across multiple cancer types. Functionally, BRD2 knockdown (KD) sensitizes tumors to the BETi JQ1, enhancing therapeutic efficacy in both *in vitro* and *in vivo* models. Mechanistically, this upregulation is driven, at least in part, by increased expression of the transcription factor NFYA. Notably, our results indicate that the extent of the initial BETi response could help predict the benefit of combining BRD2 KD with JQ1. While all BETi-treated cells gain from the combination, the most substantial enhancements are observed in resistant populations. These findings provide a rationale for incorporating BRD2 targeting into combination strategies to enhance BETi potency and prolong its clinical benefit across diverse cancers.

RESULTS

BET inhibition upregulates BRD2 across cancer types

To identify adaptive transcriptional responses to BET inhibition across cancer types, we first performed a systematic analysis of publicly available transcriptomic data. In total, we curated 51 human RNA-seq datasets following treatment with a small molecule BETi JQ1 from the Gene Expression Omnibus (GEO), published over the past decade (2014–2024), encompassing a wide spectrum of malignancies including prostate, breast, brain, skin, gastrointestinal, lung, pediatric, gynecologic and hematologic cancers (15-63). Across all datasets analyzed, *BRD2* expression was consistently and significantly upregulated upon JQ1 treatment, emerging as a recurrent transcriptional response to BET inhibition **(Fig. 1A)**. This was particularly striking given that BRD2 itself is a member of the BET protein family, alongside BRD3 and BRD4, yet was the only family member consistently induced. The strongest increase in *BRD2* expression was observed in castration resistant prostate cancer (CRPC; GSE78213), where JQ1 treatment induced a significant upregulation (log_2FC = 2.15; p-adj = 0.00), whereas *BRD3* and *BRD4* exhibited only modest changes (log_2FC = -0.13, p-adj = 0.0931; log_2FC = 0.15, p-adj = 0.561, respectively) **(Fig. 1B)**. To validate the findings from the publicly available datasets, we selected cell lines from multiple cancer types represented in the GEO analysis and assessed *BRD2* expression after JQ1 treatment. These included castration resistant prostate cancer (CRPC; PC3), hepatocellular carcinoma (HCC; Huh7), triple-negative breast cancer (TNBC; MDA-MB-231 and SUM159), glioblastoma (GBM; U251), neuroblastoma (NB; SK-N-BE2), non-small cell lung cancer (NSLC; A549), osteosarcoma (OS; U2OS), mouse and human acute myeloid leukemia (AML; RN2 and HL-60). In all cell lines tested, BRD2 protein levels were significantly increased following JQ1 treatment **(Fig. 1C; Supplementary Fig. S1A)**. Notably, BRD2 expression was generally low in leukemia cell lines that we tested. In human HL-60, BRD2 was undetectable at the protein level under baseline conditions; however, we confirmed its induction at the mRNA level in response to

JQ1. Similarly, in mouse RN2 cells, BRD2 protein became detectable only after JQ1 exposure **(Supplementary Fig. S1B)**. Collectively, these findings confirmed that BRD2 upregulation emerged as the universal response to BET inhibition, distinguishing it from other BET family members. These results suggest a previously underappreciated role for BRD2 in the context of pharmacological BET blockade and raise the possibility that its upregulation reflects a feedback or compensatory mechanism.

Pharmacological BET Inhibition, but not BRD4 depletion, induces BRD2 upregulation in pancreatic cancer

Previously, we reported that BRCA2 deficiency sensitized pancreatic ductal adenocarcinoma (PDAC) cells to BETi (64), in contrast to the general resistance observed in most PDAC cells to BETi. To further investigate the underlying mechanisms of *BRD2* upregulation upon BET inhibition, we used PDAC as a model system. In the publicly available dataset GSE192903, which profiles PANC-1 cells treated with JQ1, BRD2 was significantly upregulated ($\log_2$FC = 1.18, p-adj = 4.87×10^{-185}) **(Fig. 2A)**. To validate this, we treated 3 murine KPC pancreatic cancer cell lines (mT3-2D, mT19-2D, and mT23-2D) with JQ1 (1 μM, 24 hours) and conducted RNA-seq. Principal component analysis (PCA) revealed distinct transcriptomic shifts upon the treatment, indicating that JQ1 broadly altered the transcriptional landscape **(Supplementary Fig. S2A)**. In line with their transcriptional activation role, JQ1 treatment led to widespread gene downregulation, with 1,839 genes significantly decreased. Although *Brd3* and *Brd4* expression remained unchanged, 353 genes were significantly upregulated. Notably, *Brd2* was among the most significantly induced genes ($\log_2$FC = 2.25, p-adj = 7.16×10^{-25}) **(Fig. 2B)**. This finding was further validated by RT-qPCR and Western blot in both murine primary and metastatic PDAC cells, along with a panel of human PDAC cell lines, confirming that BRD2 upregulation is a robust and reproducible transcriptional response to BET inhibition across species and disease stages **(Fig. 2C–D; Supplementary Fig. S2B–S2D)**. Importantly, this effect

was not limited to JQ1; treatment with other small-molecule BETi—including birabresib (OTX015), molibresib (I-BET762), CPI-0610, ZEN-3694, and AZD5153—also induced BRD2 upregulation **(Fig. 2E; Supplementary Fig. S2E–S2F)**. Since BRD4 is the primary target of BETi, we next asked whether BRD2 upregulation could be induced by genetic depletion of BRD4. To test this, we knocked down BRD4 using shRNA in the same murine PDAC cell lines. Despite successfully silencing BRD4, BRD2 expression remained unchanged, highlighting that BRD4 KD elicits a different transcriptional response from pharmacological BET inhibition. **(Fig. 2F; Supplementary Fig. S2G)**. Consistent with this observation, BRD2 was upregulated by JQ1 in many various cancer models, but not by genetic depletion of BRD4 **(Supplementary Fig. S2H)** (46,54,65-68) . While the transcriptomic profile of shBRD4 cells shifted in a similar direction to that of JQ1-treated cells, the changes were less pronounced, indicating that BRD4 KD only partially phenocopies BET inhibition **(Fig. 2G)**. Together, these findings demonstrate that pharmacological BET inhibition induces BRD2 upregulation as part of a broader transcriptional response that is mechanistically distinct from BRD4 depletion, potentially reflecting an adaptive program to preserve transcriptional output.

NFYA is a putative transcriptional regulator of BRD2 upregulation in response to BET inhibition

BETi-mediated induction of BRD2 prompted us to investigate the upstream mechanisms underlying its regulation. Given that gene induction is frequently orchestrated by transcription factors (TFs), we sought to identify candidate TFs that might regulate BRD2. We began by querying the COEXPRESdb platform for transcription factors co-expressed with BRD2. Among the top 30 co-expressed genes, NFYA was the only TF identified **(Supplementary Fig. S3A–S3B)**. To further support this finding, our analysis of transcriptomic data from DepMap across 1,684 human cancer cell lines revealed a strong positive correlation between *NFYA* and *BRD2* expression (Pearson's $r = 0.628$, $p = 0.00$ **(Fig. 3A)**. We next asked whether *NFYA* and *BRD2*

are co-regulated in response to BET inhibition. Analysis of both publicly available RNA-seq datasets and our mouse PDAC dataset revealed that both *NFYA* and *BRD2* were upregulated under JQ1 treatment **(Fig. 3B; Supplementary Fig. S3A)**. To determine whether NFYA directly regulates *BRD2* transcription, we analyzed publicly available ChIP-seq datasets for NFYA. We examined NFYA binding patterns near the BRD2 gene locus to assess potential direct interaction with its regulatory regions. Indeed, NFYA consistently occupied the BRD2 promoter across multiple cell types, including leukemia, colorectal, cervical, and B lymphocytes, suggesting NFYA as a direct regulator of BRD2 **(Fig. 3C)**. To experimentally test this relationship, we performed siRNA-mediated KD of NFYA in HEK293T and U2OS cells. Depletion of NFYA reduced basal level of BRD2 expression. More importantly, NFYA depletion abrogated JQ1-mediated up-regulation of BRD2 **(Fig. 3D–E)**. Taken together, these results suggest that NFYA contributes to the transcriptional regulation of BRD2 and supports its upregulation in response to BET inhibition, highlighting NFYA as a key component of this adaptive transcriptional program.

BRD2 knockdown sensitizes cells to BET inhibition *in vitro*

Given the robust upregulation of BRD2 following BET inhibition, we hypothesized that BRD2 upregulation might confer adaptive resistance to BETi. To test this, we performed shRNA-mediated KD of BRD2 in a panel of cancer cell lines and evaluated their sensitivity to BETi. In mouse PDAC cells, Brd2 KD enhanced sensitivity to 6 different BETi–JQ1, birabresib, molibresib, ZEN-3694, CPI-0610, and AZD5153 **(Fig. 4A and B)**. Similar results were also observed in 3 additional human cancer cell lines–A549 (NSCLC), U251 (GBM), and U2OS (OS)–where BRD2 KD consistently increased JQ1 sensitivity **(Fig. 4C–H)**. Across multiple cell lines, BRD2 depletion significantly reduced IC_{50} values, indicating that BRD2 up-regulation contributes to adaptive resistance against BET inhibition. Interestingly, we observed that the magnitude of sensitization varied depending on the cell's initial response to BETi. Cells that were more resistant to BET inhibition at baseline (mT23-2D, mM1-2D, mM6-2D, and Capan-2)

exhibited a greater reduction in IC_{50} upon BRD2 KD compared to those that were initially sensitive (mT3-2D, CFPAC-1, and BxPC3) **(Fig. 4I–N, Supplementary Fig. S4A–S4C)**. In sum, our results revealed a functional role for BRD2 in mediating acute adaptive response to BETi, suggesting that targeting BRD2 enhances therapeutic efficacy, particularly in BETi-resistant tumors.

BRD2 depletion enhances BETi efficacy *in vivo*

To evaluate whether BRD2 contributes to BETi response *in vivo*, we subcutaneously injected mouse pancreatic cancer cells (mT23-2D) harboring control or BRD2-targeting shRNA into immunocompromised athymic *Nu/Nu* mice. Mice were treated intraperitoneally with either vehicle or JQ1 (50 mg/kg) over a three-week period **(Fig. 5A)**. While both JQ1 treatment alone or BRD2 KD alone moderately suppressed tumor growth, combined BRD2 KD and JQ1 treatment resulted in striking tumor growth suppression **(Fig. 5B–D)**. No overt toxicity was observed as body weight remained stable across treatment arms **(Supplementary Fig. S5)**. Immunohistochemical analysis of Ki-67 staining revealed a marked reduction in proliferative cells in BRD2 KD tumors treated with JQ1, which displayed the lowest percentage of Ki-67-positive cells and the highest proportion of Ki-67-negative cells among all groups **(Fig. 5E–F)**. Together, these results demonstrate that BRD2 depletion significantly enhances the antitumor efficacy of BET inhibition *in vivo*.

BRD2 persists on chromatin preferentially in BETi resistant cells

Given our findings that BRD2 conferred adaptive resistance to BET inhibition both *in vitro* and *in vivo*, we sought to investigate the underlying mechanisms. We first examined the basal expression levels of BRD4 and BRD2. However, we found no correlation between protein expression and JQ1 IC_{50} values **(Supplementary Fig. S6A and S6B)**, a finding corroborated by DepMap data across 394 cell lines (Pearson's r = -0.102 and

-0.058 for BRD4 and BRD2, respectively) **(Supplementary Fig. S6C and S6D)**. Therefore, we reasoned that differential BETi responses between BETi-sensitive and -resistant cells (e.g., mT3-2D (sensitive) and mT23-2D (resistant) cells) **(Fig. 6A; Supplementary Fig. S4A)** might be attributed to distinct BRD2 and BRD4 chromatin dynamics upon BETi treatment. To this end, we performed ChIP-seq for BRD2 and BRD4 in both mT3-2D and mT23-2D cells to compare their chromatin binding profiles under control and BETi conditions. Across the two cell lines, we identified 24,810 BRD4 peaks and 23,706 BRD2 peaks shared between them. Notably, there was substantial overlap in genomic occupancy: approximately 70% of BRD4-bound regions (16,941 of 24,810 peaks) were also bound by BRD2, indicating widespread co-occupancy at regulatory elements **(Fig. 6B)**, which suggests their shared roles in transcriptional regulation. As expected, JQ1 treatment led to BRD4 eviction from chromatin in both cell lines, to a similar extent. However, BRD2 remained more persistently bound in BETi-resistant mT23-2D cells compared to BETi-sensitive mT3-2D cells **(Fig. 6C)**. Similar persistence of BRD2 was observed in the TNBC cell line SUM149 upon BET inhibition, as previously reported, suggesting a broader relevance across cancer types **(Supplementary Fig. S6E)**. This prompted us to ask whether transcriptional activity was maintained at regions where BRD4 was displaced but BRD2 remained bound. Analysis of the top 1,000 JQ1-sensitive BRD2 peaks in sensitive mT3-2D cells revealed that BRD2 occupancy at these loci persisted prominently in resistant mT23-2D cells. Overlaying this with our RNA-seq data revealed that many genes affected by BRD4 displacement in sensitive cells continued to be expressed in resistant cells, implying that BRD2 retention may compensate for BRD4 loss to preserve transcriptional output. To further understand the biological implications of this compensatory effect, we performed GO Biological Process (GOBP) analysis on genes that were highly affected by JQ1 in sensitive cells but remained transcriptionally active in resistant ones. The enriched categories included chromatin organization, RNA processing, histone modification, mRNA splicing, and post-transcriptional regulation of gene expression **(Fig. 6E; Supplementary Fig. S6F)**. These pathways represent

essential gene regulatory and epigenetic processes, consistent with the idea that BRD2 occupancy at chromatin helps preserve core transcriptional and biosynthetic programs. Our findings suggest that upon BET inhibition, BRD2 retention enables BETi-resistant cells to sustain the hyper-transcriptional state characteristic of cancer,thereby maintaining transcriptional activity despite BRD4 displacement from chromatin. These observations highlight BRD2 as a critical compensatory factor in BETi resistance and suggest that BRD2 targeting strategy either directly or in combination with BETi may enhance treatment efficacy.

DISCUSSION

BRD4 dependency in many cancers, including leukemia, provided the rationale for developing BETi. The first-generation inhibitor JQ1 demonstrated potent anti-tumor effects in preclinical models such as NUT carcinoma and MYC-driven leukemia. However, its poor bioavailability, short half-life, and off-target toxicities limited its clinical use, prompting the development of second-generation BETi with improved pharmacokinetics, enhanced specificity, and orally available formulations. Indisputably, despite these advances, cancer cells can activate alternative pathways to circumvent therapy, mitigating its effects and sustaining survival. These adaptive responses not only represent tangible vulnerabilities but, when understood, can also be exploited to prevent resistance and achieve better therapeutic outcomes. Several studies have informally noted increased BRD2 expression following BETi treatment, but it has remained unclear whether this functionally confers adaptive resistance across pan-cancers. Recent synthetic lethal screens with BETi in TNBC and paralog-focused CRISPR screens in lung, skin, pancreas and brain cancers, have independently identified BRD2 as a potential resistance factor (69,70). Yet, the role of BRD2 has not been systematically examined. Here, we show that transcriptional upregulation of BRD2 is a robust adaptive response to BETi across diverse cancer types, and that BRD2 depletion sensitizes cells to BET inhibition both *in vitro* and *in vivo*.

Paralog compensation is an emerging theme in targeted cancer therapy, wherein inhibition of one protein prompts adaptive up-regulation of a closely related family member that compensates for its function. For example, EZH2 inhibition in malignant rhabdoid tumors has been shown to induce EZH1 upregulation, and dual EZH1/2 inhibition yields improved therapeutic responses (71). Similarly, inhibition of the histone demethylase LSD1 (KDM1A) in Ewing sarcoma cells resulted in marked induction of its homolog LSD2 (KDM1B), a shift that modulates drug sensitivity (72). Recent large-scale paralog-focused CRISPR screens have uncovered multiple additional examples of this phenomenon, such as the reciprocal buffering

between DUSP4 and DUSP6 (70). Here, we present the first comprehensive evidence that BRD2 upregulation is a highly conserved and universal adaptive response to BET inhibition across cancer types, functionally analogous to other paralog compensation events where BRD2 substitutes for BRD4 to preserve transcriptional programs upon BET inhibition.

Our data suggest that resistance is mediated in part through paralog redundancy, with BRD2 compensating for BRD4 function under BET inhibition. This compensatory role aligns with their shared canonical functions in transcriptional regulation, as evidenced by their largely overlapping genomic occupancy (69). However, BRD2 also carries out distinct functions that may independently and uniquely support adaptive resistance. Upon JQ1 treatment, BET proteins can remain in the nucleus and, through their ET domains, may exert bromodomain-independent functions that sustain cell survival. Unlike BRD4, BRD2 is closely associated with chromatin architectural regulation: it co-localizes genome-wide with CTCF, contributes to the maintenance of topologically associating domain (TAD) boundaries, and influences compartmentalization of the accessible genome (73,74). C-terminal domain of BRD2 also mediates critical protein-protein interactions, enabling recruitment to promoters and CTCF-bound sites. The unique roles of BRD2 raise the possibility that its upregulation under BET inhibition may confer survival advantages beyond its role in transcriptional regulation.

Our findings suggest a therapeutic opportunity to enhance BETi efficacy by preventing or counteracting BRD2 upregulation. This could be achieved either through selective BRD2 inhibition in combination with conventional BETi which predominantly target BRD4 or by strategies that broadly degrade BET family members to prevent compensatory mechanisms. PROTAC-based BET degraders, which remove BRD2, BRD3, and BRD4 from chromatin, have recently demonstrated superior antitumor activity compared to earlier generations of BETi (58,75). Notably, the absence of BRD2 upregulation in PROTAC-based approaches may partially explain their improved efficacy. While additional resistance mechanisms undoubtedly exist, our

data highlight BRD2 compensation as a conserved and targetable pathway. As a proof-of-principle, we show that BRD2 depletion sensitize tumors to BET inhibition. This provides a rationale for integrating BETi with approaches that mitigate BRD2-driven adaptive resistance could achieve more durable clinical responses and expand the therapeutic potential of BET-targeted strategies in cancer therapeutics.

FIGURE LEGEND

Figure 1 BRD2 upregulation in pan-cancer upon BET inhibition. A, Dot plots showing *BRD2* expression changes (JQ1 vs. control) across 51 curated human RNA-seq datasets from GEO (2014–2024), including gastrointestinal, breast, prostate, skin, brain, lung, pediatric, gynecologic, and hematologic cancers. The x-axis indicates $\log_2$(Fold change), and dot size represents statistical significance (-$\log_{10}$adjusted p-value). Abbreviations: CRPC, castration-resistant prostate cancer; TNBC, triple-negative breast cancer; ER+, estrogen receptor–positive; BC, breast cancer; GBM, glioblastoma; NB, neuroblastoma; MEL, melanoma; HNSCC, head and neck squamous cell carcinoma; CRC, colorectal cancer; PDAC, pancreatic ductal adenocarcinoma; GIST, gastrointestinal stromal tumor; HCC, hepatocellular carcinoma; SCLC, small cell lung cancer; NSCLC, non–small cell lung cancer; RMS, rhabdomyosarcoma; AT/RT, atypical teratoid/rhabdoid tumor; ES, Ewing sarcoma; OC, ovarian cancer; CC, cervical cancer; MM, multiple myeloma; T-ALL, T-cell acute lymphoblastic leukemia; CML, chronic myeloid leukemia; BL, Burkitt lymphoma; AML, acute myeloid leukemia. **B,** Volcano plot of differentially expressed genes in castration resistant prostate cancer (GSE78213), highlighting robust BRD2 upregulation upon JQ1 treatment. BRD3 and BRD4 remained unaffected. **C,** Western blot validation showing BRD2 protein levels in multiple representative human cell lines from prostate (PC3), liver (Huh7), breast (MDA-MB-231), brain (U251), lung (A549), and pediatric (U2OS) cancers with and without 10 μM JQ1 for 24 hours.

Figure 2 Pharmacological BET inhibition uniquely drives BRD2 upregulation in pancreatic cancer A, Volcano plot of differentially expressed genes in human PDAC (PANC-1; GSE192903) treated with JQ1, highlighting strong upregulation of BRD2, not BRD3 nor BRD4. **B,** Volcano plot of RNA-seq data from murine PDAC cells (mT3-2D, mT19-2D, mT23-2D) treated with JQ1 (1 μM, 24 hours), showing conserved BRD2 induction. **C,** Western blot validation of BRD2 upregulation in murine PDAC cell lines (mT19-2D, mT23-2D, mM6-2D, mM10-2D) treated with

JQ1 (1 μM, 24 hours). **D,** Western blot analysis in a panel of human PDAC cell lines (MIAPaCa-2, PANC-1, Capan-2, AsPC-1, SUIT-2, PaTu8988s, HPAF-II, CFPAC-1) confirming JQ1-induced BRD2 expression. **E,** Western blot analysis of BRD2 in mT23-2D cells treated for 24 hours with different small-molecule BET inhibitors (JQ1, Birabresib, Molibresib, CPI-0610, AZD5153 at 1 μM; ZEN-3694 at 5 μM), showing a consistent increase in BRD2 expression across inhibitors. **F,** Western blot analysis of BRD2 expression following shRNA-mediated BRD4 knockdown (KD) in murine (mT3-2D, mT23-2D) and human (SUIT-2, CFPAC-1) PDAC cell lines, revealing that BRD4 depletion does not mimic JQ1-induced BRD2 upregulation. **G,** Principal component analysis (PCA) of RNA-seq data from murine PDAC cells (mT3-2D, mT19-2D, mT23-2D) under DMSO, JQ1, shScr, or shBrd4 conditions, showing distinct transcriptional clustering of JQ1-treated samples compared to BRD4 KD.

Figure 3 NFYA as a candidate transcriptional regulator of BRD2 induction upon BET inhibition. A, Scatterplot from DepMap analysis showing a positive correlation between NFYA and BRD2 expression across public cancer transcriptomes. **B,** Representative 3D volcano plot of publicly available RNA-seq datasets treated with JQ1, highlighting recurrent co-upregulation of *BRD2* and *NFYA*. **C,** NFYA ChIP-seq profiles at the BRD2 locus across multiple human cell types (K562 leukemia, lymphocytes, cervical cancer, colorectal cancer), demonstrating NFYA occupancy at the BRD2 promoter. **D and F,** Western blot analysis of NFYA and BRD2 in HEK293T (D) and U2OS (F) cells transfected with control siRNA (siNeg) or NFYA siRNA (siNFYA) and treated with DMSO or JQ1 (1 μM, 24 hours). **E and G,** RT-qPCR quantification of BRD2 expression in HEK293T (E) and U2OS (G) cells under the same conditions, showing that NFYA KD attenuated JQ1-mediated BRD2 upregulation. Statistical significance was determined by one-way ANOVA (*$p < 0.05$, **$p < 0.01$, ***$p < 0.001$, ****$p < 0.0001$).

Figure 4 BRD2 depletion sensitizes cancer cells to BET inhibition. A, Immunoblot confirming BRD2 KD in mT23-2D PDAC cells (shScr vs shBrd2). **B,** Dose–response curves showing reduced

cell viability upon treatment with various BETi (JQ1, Birabresib, Molibresib, ZEN-3694, CPI-0610, AZD5153) in BRD2-depleted mT23-2D cells compared to controls. **C–D,** Immunoblot (C) and JQ1 dose–response curve (D) in lung cancer (A549) cells with BRD2 KD. **E–F,** Immunoblot (E) and JQ1 dose–response curve (F) in brain cancer (U251) cells. **G–H,** Immunoblot (G) and JQ1 dose–response curve (H) in pediatric cancer (U2OS) cells. **I–N,** Immunoblot (I, J, K) and JQ1 dose–response curves (L, M, N) in PDAC cell lines Capan-2, CFPAC-1, and BxPC-3 upon BRD2 KD.

Figure 5 Genetic BRD2 perturbation enhances the antitumor effect of BET inhibition *in vivo*. A, Schematic of in vivo experimental design, created with Biorender. KPC pancreatic tumor cells transduced with shScr or shBrd2 were injected subcutaneously into the flanks of mice. Animals were randomized into vehicle or JQ1 treatment groups (50 mg/kg, intraperitoneally, daily). **B,** Representative images of mice and excised tumors from each group after treatment. **C,** Tumor growth curves over time showing significantly impaired tumor growth in shBrd2 + JQ1 tumors compared to controls. Error bars represent SD. **D,** Tumor weight at endpoint, showing that shBrd2 + JQ1 tumors had the lowest weights. Statistical significance was determined by two-tailed Student's t-test (****$p < 0.0001$). **E–F,** Representative and quantification Ki67 immunohistochemistry of tumors showing reduced proliferative index in shBrd2 + JQ1 tumors.

Figure 6 BRD2 retention sustains transcriptional programs in BET inhibitor–resistant pancreatic cancer cells. A, Dose–response curves comparing BETi sensitivity (JQ1, Molibresib, Birabresib) in sensitive (mT3-2D) and resistant (mT23-2D) PDAC cells. IC_{50} values are shown in the table. **B,** Venn diagram of BRD4 and BRD2 ChIP-seq peaks in mT3-2D and mT23-2D cells, showing extensive overlap but also unique binding sites for each factor. **C,** ChIP-seq density and heatmaps of BRD4 and BRD2 binding at shared peaks in sensitive (mT3-2D) and resistant (mT23-2D) cells treated with DMSO or JQ1. While BRD4 occupancy is reduced upon JQ1 treatment, BRD2 binding persists in resistant cells. **D,** Heatmap of representative genes associated with JQ1-sensitive BRD4 peaks in mT3-2D that remain active in mT23-2D, consistent

with BRD2 retention. **E,** GOBP (GREAT analysis) of the top 1,000 BRD2-bound regions in resistant cells, highlighting categories involved in chromatin organization, RNA processing, histone modification, and biosynthetic pathways. **F,** Proposed schematic model illustrating BRD2 upregulation as an adaptive mechanism to BET inhibition.

Supplementary Figure 1 BRD2 upregulation by JQ1 across additional cancer types. A, Western blot analysis of BRD2 in brain cancer (SK-N-BE2) and breast cancer (SUM159) cells treated with DMSO or JQ1. **B–C,** RT-qPCR and immunoblot analysis of BRD2 expression in human and mouse blood cancer (HL-60, RN2) cells, showing increased BRD2 levels upon JQ1.

Supplementary Figure 2 BRD2 induction by BET inhibition but not by BRD4 KD. A, PCA of RNA-seq profiles from murine PDAC cell lines (mT3-2D, mT19-2D, mT23-2D) treated with DMSO or JQ1, showing distinct clustering of JQ1-treated samples. **B,** RT-qPCR analysis of BRD2 expression in multiple murine and human PDAC cell lines treated with JQ1, revealing significant induction across models. Statistical significance was determined using a two-tailed Student's t-test (***$p < 0.001$, ****$p < 0.0001$) **C–D,** Western blot analysis of BRD2 and BRD4 expression in murine (mT3-2D, mM1-2D) and human (BxPC-3, Capan-1) PDAC cells after JQ1 treatment. **E,** Immunoblot analysis of BRD2 and BRD4 expression following treatment with JQ1, Birabresib or Molibresib in mouse PDAC mT3-2D and mT19-2D cells. **F,** Western blot analysis of BRD2 expression in murine PDAC cell lines (mT4-2D, mT5-2D, and mT8-2D) treated with different BET inhibitors (JQ1, Birabresib, Molibresib, ZEN-3694, CPI-0610, AZD5153; 1 μM, 24 hours), showing consistent BRD2 upregulation across inhibitors compared with control. **G,** Western blot analysis of BRD2 expression after shRNA-mediated BRD4 KD in PDAC AsPC-1 and breast cancer SUM159 cells, showing that BRD4 depletion did not result in BRD2 induction by JQ1. **H,** Analysis of publicly available RNA-seq datasets (GEO) across multiple cancer types (rhabdomyosarcoma, embryonic kidney, liver cancer, breast cancer, PDAC, and Ewing sarcoma), showing that BRD4

KD generally does not increase *BRD2* expression, whereas JQ1 significantly induces *BRD2*. Statistical significance was determined by two-tailed Student's t-test (**$p < 0.01$).

Supplementary Figure 3 NFYA emerges as a candidate regulator of BRD2. A, List of top 30 BRD2-interacting transcriptional regulators identified from COEXPRESdb. **B,** Co-expression analysis of NFYA and BRD2 using COEXPRESdb, showing a strong positive correlation across transcriptomes ($z = 5.62$). **C,** RNA-seq analysis of *Nfya* expression in mouse PDAC cells treated with DMSO or JQ1, showing significant *Nfya* upregulation upon JQ1 treatment (***$p < 0.001$).

Supplementary Figure 4 BRD2 KD enhances sensitivity to BET inhibition across murine PDAC models. A–C, Immunoblot validation of BRD2 KD (shBrd2 vs. shScr control) in mT3-2D (A), mM1-2D (B), and mM6-2D (C) murine PDAC cell lines. Dose–response curves with JQ1 showed that BRD2 depletion sensitizes all three PDAC models to BET inhibition.

Supplementary Figure 5 Body weight (BW) was maintained during JQ1 treatment. A, BW of mice bearing tumors treated with vehicle or JQ1. No significant weight loss was observed.

Supplementary Figure 6 Basal BRD4/BRD2 levels and chromatin occupancy do not predict JQ1 response. A–B, Correlation analyses between basal BRD4 (A) or BRD2 (B) mRNA expression levels and JQ1 sensitivity across human PDAC cell lines. No significant associations were observed. **C–D,** Correlation of BRD4 (C) and BRD2 (D) expression levels with JQ1 sensitivity across public cancer transcriptome datasets. Both factors showed weak or no predictive value. **E,** Venn diagram of BRD2 and BRD4 ChIP-seq binding regions in breast cancer cells (GSE131097), highlighting substantial overlap. Metaprofiles of BRD4 (left) and BRD2 (right) occupancy at BRD4-bound sites under DMSO or JQ1 conditions, suggesting BRD2 binding persists at regions where BRD4 occupancy is displaced upon JQ1. **F,** GOBP enrichment (ShinyGO) of the top 1,000 JQ1-responsive BRD2-bound regions annotated by GREAT, revealing significant enrichment for RNA metabolic and biosynthetic processes.

Materials and methods

Cell lines and cell culture condition

A diverse panel of mouse and human cancer cell lines was used in this study. All cells were maintained at 37°C in a humidified incubator with 5% CO_2 under standard conditions appropriate for each cell type. The base culture media included Dulbecco's Modified Eagle Medium (DMEM; Corning, 10-013-CV), RPMI-1640 (Gibco, 11875119), Iscove's Modified Dulbecco's Medium (IMDM; Gibco, 12440053), McCoy's 5A Modified Medium (Gibco, 16600082), Eagle's Minimum Essential Medium (EMEM; ATCC, 30-2003), and Advanced DMEM/F-12 (Gibco, 12634028). Unless otherwise specified, culture media were supplemented with 10% fetal bovine serum (FBS; GenClone, 25-550H) and 1% penicillin-streptomycin (P/S; Gibco, 15140-122). Triple-negative breast cancer (TNBC) cell lines were additionally supplemented with 10 mM HEPES (Gibco, 15630080), 1 μg/ml hydrocortisone, and 5 μg/ml insulin (Sigma-Aldrich, I0516-5ML). Cell line information, including species, tumor type, tissue origin, and specific culture conditions, is listed in the table below.

Mouse pancreatic cancer cell lines (76)

Cell Line			Culture Medium
mT3-2D	mT4-2D	mM1-2D	DMEM + 10% FBS + 1% P/S
mT19-2D	mT5-2D	mM6-2D	
mT23-2D	mT8-2D		

Human pancreatic cancer cell lines

Cell Line	Culture Medium
AsPC-1	RPMI-1640 + 10% FBS + 1% P/S
CFPAC-1	
MIA PaCa-2	
PANC-1	
PaTu8988s	
SUIT-2	
Capan-2	McCoy's 5A + 10% FBS + 1% P/S
HPAF-II	EMEM + 10% FBS + 1% P/S

Other mouse cancer cell lines

Cell Line	Tumor Type	Tissue Origin	Culture Medium
RN2	Acute myeloid leukemia	Bone marrow	DMEM + 10% FBS + 1% P/S

Other human cancer cell lines

Cell Line	Tumor Type	Tissue Origin	Culture Medium
A549	Non-small cell carcinoma	Lung	DMEM + 10% FBS + 1% P/S
Huh7	Hepatocellular carcinoma	Liver	
PC3	Prostate adenocarcinoma	Prostate	
SK-N-BE2	Neuroblastoma	Brain	
U251	Glioblastoma	Brain	
U2OS	Osteosarcoma	Bone	McCoy's 5A + 10% FBS + 1% P/S
HL-60	Acute myeloid leukemia	Bone marrow	RPMI-1640 + 10% FBS + 1% P/S
SUM159	Triple-negative breast cancer	Breast	Advanced DMEM/F-12 + 5% FBS + 10mM HEPES + 1μg/ml hydrocortisone + 5μg/ml insulin
MDA-MB-231	Triple-negative breast cancer	Breast	

Compounds

All compounds were purchased from the indicated suppliers below and dissolved in dimethyl sulfoxide (DMSO; Sigma-Aldrich, 472301-500ML) prior to use.

Compound Name	Source	Catalog Number
JQ1	MedChemExpress	ML-13030
Molibresib (I-BET762)	MedChemExpress	ML-13032
Birabresib (OTX-015)	MedChemExpress	ML-15743
AZD5153	MedChemExpress	ML-100653
CPI-203	MedChemExpress	ML-15846
ZEN-3694	Selleckchem	E1517

Cell viability assay

Mouse cancer cells (1,500 cells/well) or human cancer cells (3,000 cells/well) were seeded in 50 μl of complete DMEM into 96-well plates. After 24 hours, drugs were serially diluted in complete DMEM and 50 μl of the diluted compounds were added to each well. Cells were incubated for an additional 72 hours before media were carefully removed. To assess cell

viability, 100 µl of diluted AlamarBlue solution prepared by mixing 200 µl of resazurin (Fisher Scientific, AC418900010) in 50 ml of 1× PBS was added to each well. Plates were incubated at 37°C with 5% CO_2 for 3-4 hours. Absorbance at 570 nm was measured using a plate reader (SpectraMax iD5 plate reader, Molecular Devices). Relative cell viability was calculated by normalizing the absorbance of drug-treated wells to vehicle-treated controls. Dose-response curves were generated using nonlinear regression (curve fitting) in GraphPad Prism.

shRNA construct generation via pLKO.1 cloning

For the generation of shRNA constructs, the pLKO.1-puro vector (Addgene #8453) was used. A total of 6 µg of plasmid DNA was digested with 1 µl EcoRI-HF (NEB, R3101T), 1 µl AgeI-HF (NEB, R3552S), and 5 µl rCutSmart Buffer (NEB, B6004S) in a 50 µl reaction and incubated at 37°C for 3 hours. To prevent vector self-ligation, 1 µl Quick CIP (NEB, M0525S) was added and incubated for an additional hour at 37°C. The digested vector was purified using the PureLink PCR purification kit (Invitrogen, K310002). For oligonucleotide preparation, 1 µl of forward and reverse primers (each at 100 µM) were combined with 1 µl 10× T4 DNA ligase buffer (NEB, B0202S), 0.5 µl T4 Polynucleotide Kinase (NEB, M0201S), and 6.5 µl nuclease-free water. The reaction was incubated at 37°C for 30 minutes, then heated to 95 °C for 5 minutes, followed by a gradual ramp down to 25°C at 5 °C/min for annealing. The annealed primers were diluted 1:200 before ligation. Ligation reactions were performed by mixing 50 ng of digested pLKO.1 vector, 1 µl diluted annealed oligos, 1 µl 10× T4 ligase buffer (NEB, B0202S), 1 µl T4 DNA ligase (NEB, M0202S), and water to a final volume of 10 µl. The mixture was incubated at room temperature for 30 minutes. For transformation, 3 µl of the ligation mix was added to 30 µl XL10-Gold ultracompetent cells (Agilent, 50-125-094). After 5 minutes on ice, cells were heat-shocked at 42°C for 90 sec, returned to ice for another 5 minutes, and plated on LB agar (Fisher Scientific, BP1427-500) supplemented with 1× ampicillin (RPI, C802G69) using 4.5 mm sterile rattler plating beads (Zymo Research, S1001). Plates were incubated overnight at 37°C (~16 hours).

At least 6 individual colonies were miniprepped, and plasmid inserts were verified by Sanger sequencing (GENEWIZ) using primers targeting the U6 promoter. Resulting sequences were aligned to reference in Benchling to confirm correct oligo insertion. Information about the short hairpin RNA (shRNA) constructs used in this study, including the target gene, sequence ID, and oligonucleotide sequences, is summarized in the table below.

Mouse

shRNA Construct	Target Sequence ID	Sequence (5' → 3')	
shBrd2	TRCN0000362395	Forward	CCGGCCCTCTCTACGTGATTCAAATCTCGAGATTTGAATCACGTAGAGAGGGTTTTTG
		Reverse	AATTCAAAAACCCTCTCTACGTGATTCAAATCTCGAGATTTGAATCACGTAGAGAGGG
shBrd4	TRCN0000088480	Forward	CCGGGCGGCAGCTAAGTCTAGATATCTCGAGATATCTAGACTTAGCTGCCGCTTTTTG
		Reverse	AATTCAAAAAGCGGCAGCTAAGTCTAGATATCTCGAGATATCTAGACTTAGCTGCCGC

Human

shRNA Construct	Target Sequence ID	Sequence (5' → 3')	
shBRD2	TRCN0000006310	Forward	CCGGCCCTGCCTACAGGTTATGATTCTCGAGAATCATAACCTGTAGGCAGGGTTTTTG
		Reverse	AATTCAAAAACCCTGCCTACAGGTTATGATTCTCGAGAATCATAACCTGTAGGCAGGG
shBRD4	TRCN0000021427	Forward	CCGGCCTGGAGATGACATAGTCTTACTCGAGTAAGACTATGTCATCTCCAGGTTTTTG
		Reverse	AATTCAAAAACCTGGAGATGACATAGTCTTACTCGAGTAAGACTATGTCATCTCCAGG

Lentiviral production and transduction

Lentiviral particles were produced by transfecting HEK293T cells using a standard third-generation packaging system. Briefly, 5×10^6 HEK293T cells were seeded in 10 cm culture dishes. After 18-24 hours, the medium was replaced with DMEM supplemented with 10% FBS (without P/S). Cells were then transfected with 10 μg of transfer plasmid (e.g., shRNA

constructs), 8 μg of psPAX2 (Addgene #12260), and 2 μg of pMD2.G (Addgene #12259), using X-tremeGENE 360 transfection reagent (Roche, 8724156001) at a 1:3 DNA-to-reagent ratio, following the manufacturer's instructions. After 48-72 hours, the viral supernatant was collected, centrifuged at 1,100 rpm for 5 minutes to remove cell debris, and filtered through a 0.45 μm PES filter (Cytiva, 28143-312). The resulting virus-containing media were used to transduce target cells in the presence of polybrene (MilliporeSigma, C788D57) at a final concentration of 1 μg/ml. Twenty-four hours after transduction, cells were selected with 2 μg/ml puromycin (Thermo Scientific, 53-79-2) for at least 72 hours. Successful gene knockdown was subsequently validated by western blot, confirming effective transduction and target suppression.

siRNA transfection

NFYA-specific siRNAs (sc-29947) and non-silencing control siRNA (sc-37007) were purchased from Santa Cruz Biotechnology. Cells were transfected with 40 nM siRNA using X-tremeGENE 360 reagent (Roche, 8724156001) following the manufacturer’s protocol. After 48 hours, transfected cells were treated with JQ1 (1 μM) for 24 hours, and NFYA knockdown efficiency was assessed by Western blot.

Western blotting

Cells at 80–90% confluency were scraped on ice using a cell lifter (Biologix, 70-2180) into lysis buffer (50 mM Tris, pH 7.5; 150 mM NaCl; 5 mM EDTA; 1% Triton X-100) supplemented with protease inhibitor cocktail (Sigma-Aldrich, SIAL-11836170001) and phosphatase inhibitor cocktail (Roche, 04906837001). Lysates were incubated on ice for 30 minutes and then clarified by centrifugation at 14,000 rpm for 10 minutes at 4°C. Supernatants were transferred to fresh tubes, and protein concentrations were measured using the DC Protein Assay Kit (Bio-Rad; Reagents A, B, S: 5000113, 5000114, 5000115). A total of 20 μg of protein was mixed with 4× LDS sample buffer (Invitrogen, B0007) and 10× NuPAGE Sample Reducing Agent (Invitrogen,

NP0009), adjusted to a final volume of 20 µl, and heated at 70°C for 10 minutes. Samples were loaded onto 4-12% Bis-Tris NuPAGE gels (Invitrogen, NP0321) and electrophoresed using a Minutes Gel Tank (Thermo Fisher, A25977) in MES SDS Running Buffer (Invitrogen, NP0002) at 120 V for 90 minutes. Proteins were transferred to 0.45 µm PVDF membranes (Millipore, IPVH00010) at 350 mA for 150 minutes at 4°C. Membranes were blocked in 5% skim milk prepared in Tris-buffered saline with 0.1% Tween-20 (TBST) for 1 hour at room temperature. They were then incubated overnight at 4°C with primary antibodies diluted in 5% skim milk in TBST under gentle agitation (~70 rpm) (ONILAB, SK-O180-S). Following incubation, membranes were washed three times for 10 minutes each with 1× TBST on a rocker and then incubated with HRP-conjugated secondary antibodies (1:5000 dilution) in the same blocking buffer for 1 hour at room temperature. Membranes were subsequently washed three more times for 10 minutes with TBST. Signal was detected using SuperSigna West Femto Maximum Sensitivity Substrate (Thermo Scientific, 34094) and visualized using the Amersham Imager 600 (GE Healthcare Life Sciences).

Antibody	Source	Catalog Number	Dilution
BRD2	Cell Signaling Technology	5848S	1:1000
BRD4	Novus Biologicals	NBP2-76393	1:1000
GAPDH	ProSci	3783	1:1000
Vinculin	Cell Signaling Technology	13901	1:1000
Donkey anti-rabbit IgG (MINUTES+L) HRP	Invitrogen	A16023	1:5000

Animal studies and treatment regimen

Female athymic nude (Nu/Nu) mice (6 weeks old) were obtained from the Jackson Laboratory and housed under specific pathogen-free conditions in the Genome and Biomedical Sciences Facility at the University of California, Davis. Mice were maintained with controlled ambient temperature and a standard light–dark cycle. All procedures were approved by the Institutional Animal Care and Use Committee (IACUC). JQ1 (MedChemExpress, ML-13030) was prepared

by dissolving the drug in DMSO (Sigma-Aldrich, 472301-500ML), then diluting in vehicle composed of 95% of a 20% SBE-β-CD solution (MedChemExpress, MINUTES-17031) in saline (Moltox, C790D04) to a final concentration of 5 mg/ml. For subcutaneous tumor engraftment, cells were trypsinized, passed through a 40 μm cell strainer (Biologix, 15-1040), and resuspended in 50 μl of Cultrex Reduced Growth Factor Basement Membrane Extract (Bio-Techne, 3533-010-02). Each mouse received 0.5×10^6 cells: shScr control cells in the left flank and shBrd2 cells in the right flank. Three days post-engraftment, mice were randomized into two treatment groups (n = 10 per group) and administered either vehicle or JQ1 intraperitoneally at 50 mg/kg, five times per week. Tumor size was measured using Vernier calipers three times per week, and tumor volume was calculated as: $(\pi \times \text{length} \times \text{width}^2)/6$. At the end of the treatment period, mice were euthanized, and tumors were harvested for histological analysis.

Histology and immunohistochemistry

Harvested tumors were fixed in 10% neutral buffered formalin and replaced with 70% ethanol on the following day. Formalin-fixed paraffin-embedded (FFPE) sections with 5 μm thickness were prepared for and immunohistochemistry. For immunohistochemical staining on Ki67, antigen retrieval was performed for 45 minutes with citrate buffer at pH 6.0 in a Decloaking Chamber (Biocare Medical) at 125°C and 15 psi. Slides were blocked with normal goat serum then incubated with rabbit polyclonal Ki67 (NeoMarkers, RB1510P, 1:1000 dilution) overnight at room temperature in a humidified chamber, followed by biotinylated goat anti-rabbit secondary antibody (1:1000 dilution). The Vectastain ABC kit elite kit and diaminobenzidine peroxidase substrate kit (Vector Labs) were used for amplification and visualization of signal, respectively.

RNA extraction

Cells were lysed in 1 ml of TRIzol reagent (Thermo Fisher Scientific, 15596026) at room temperature for 5 minutes with gentle agitation, followed by the addition of 200 μl of chloroform

(Reagents, C755N59), according to the manufacturer's protocol. RNA was extracted using the PureLink RNA Mini Kit (Invitrogen, 12183018A) and quantified using a NanoDrop ND-1000 spectrophotometer (Thermo Scientific) prior to sequencing submission.

Reverse transcription quantitative PCR (RT-qPCR)

Total RNA was extracted using TRIzol reagent (Invitrogen, 15596026). After 5 minutes of incubation at room temperature, 200 µl of chloroform (Reagents, C755N59) was added, and samples were vigorously mixed until homogeneous, followed by 5 minutes on ice. Samples were centrifuged at 14,000 rpm for 15 minutes at 4°C, and the aqueous phase was transferred to a new DNase/RNase-free tube. RNA was further purified using the PureLink RNA Minutes Kit (Invitrogen, 12183018A), including on-column DNase treatment (PureLink DNase Set, Invitrogen, 12185010). RNA was eluted in nuclease-free water, and concentration and purity were assessed using a NanoDrop ND-1000 spectrophotometer (Thermo Scientific). cDNA synthesis was performed with the High-Capacity cDNA Reverse Transcription Kit (Applied Biosystems, 4368814) using 1 µg of total RNA per 20 µl reaction. The reaction mix included 3 µl 10× RT buffer, 1.2 µl 25X dNTP mix, 3 µl 10× random primers, 1.5 µl MultiScribe reverse transcriptase, and 6.3 µl nuclease-free water. The thermocycling conditions were: 25°C for 10 minutes, 37°C for 120 minutes, and 85°C for 5 minutes. qPCR was performed using 1 µl of cDNA with PowerTrack SYBR Green Master Mix (Applied Biosystems, A46109) and gene-specific primers in a total reaction volume of 10 µl. Reactions were run on a LightCycler 480 system (Roche) with the following setting: 95°C for 10 minutes, followed by 40 cycles of 95°C for 15 seconds and 60°C for 60 seconds. Relative mRNA expression levels were normalized to *GAPDH* (human samples) or *Gapdh* (mouse samples) and calculated using the $2^{-\Delta\Delta Ct}$ method.

Primer list

Brd2	Forward	ATGCTGCAAAACGTGACTCC
Brd2	Reverse	AAGCTGGTACAGAAGCCATTG
Brd4	Forward	AGTGTCTTTGACCCTATTAGCCA
Brd4	Reverse	CATGCTGGTTGAGATGGGG
Gapdh	Forward	TTCACCACCATGGAGAAGGC
Gapdh	Reverse	CCCTTTTGGCTCCACCCT
BRD2	Forward	CGGCTTATGTTCTCCAACTGCTA
BRD2	Reverse	GGCAGTAGAGACTGGTAAAGGC
BRD4	Forward	ACCTCCAACCCTAACAAGCC
BRD4	Reverse	TTTCCATAGTGTCTTGAGCACC
GAPDH	Forward	CCAAGGAGTAAGACCCCTGG
GAPDH	Reverse	AGGGGAGATTCAGTGTGGTG

Chromatin immunoprecipitation sequencing (ChIP-seq)

For ChIP-seq, approximately 1 × 10^7 cells were harvested per sample using TrypLE Express Enzyme (Gibco, 12605028) and resuspended in PBS to generate a single-cell suspension. Chromatin immunoprecipitation was carried out using the SimpleChIP® Enzymatic Chromatin IP Kit (Magnetic Beads) (Cell Signaling Technology, #9003) according to the manufacturer's protocol with minor modifications. Briefly, cells were fixed in 1% formaldehyde at room temperature for 10 minutes to crosslink protein-DNA interactions. Crosslinking was quenched with glycine (final concentration 125 mM) for 5 minutes at room temperature. Cells were then washed twice with ice-cold PBS and lysed in lysis buffer to isolate nuclei. Chromatin was enzymatically digested with 1 µl of micrococcal nuclease (MNase) at 37°C for 20 minutes to achieve partial digestion, followed by mechanical shearing using a Bioruptor (Diagenode) set to high power for 3 rounds of 10 cycles (30 seconds on, 30 seconds off). Shearing was performed in 1.5 ml TPX microtubes (Diagenode, C30010010) to generate DNA fragments ranging from 150 to 500 bp. DNA fragmentation was verified by 1.8-2% agarose gel electrophoresis. For immunoprecipitation, 10 µl of antibody was used per reaction: BRD2 (Cell Signaling Technology, 5848S) or BRD4 (Bethyl Laboratories, A301-985A100). Chromatin and protein G magnetic beads were incubated overnight at 4°C with antibodies under constant agitation using a tube

rotator to promote optimal antigen-antibody interaction. Beads were then washed sequentially with low salt, high salt, and LiCl wash buffers, followed by TE buffer. Crosslinks were reversed by incubating with Proteinase K at 65°C for 2 hours. DNA was purified using spin columns included in the kit according to the manufacturer's instructions (Cell Signaling Technology, 14209S).

Library preparation and sequencing

Library preparation and sequencing for ChIP-seq and RNA-seq were carried out by Novogene Co., LTD. For ChIP-seq, sample quality was assessed prior to library construction. DNA fragments were end-repaired, A-tailed, and ligated to Illumina adapters, followed by size selection, PCR amplification, and quantification. Libraries were sequenced on an Illumina NovaSeq X Plus platform (PE150). Quality control procedures, including assessments of sequencing quality distribution, error rate distribution, and AT/CG base composition, were performed before data delivery. For RNA-seq, total RNA quality was assessed using 1% agarose gel electrophoresis, NanoDrop spectrophotometry (for RNA quantity and purity), and an Agilent 2100 Bioanalyzer (for RNA Integrity Number, RIN). Poly(A) mRNA was enriched from total RNA using oligo(dT) magnetic beads, fragmented, and reverse-transcribed to synthesize first-strand cDNA with random primers. Second-strand cDNA synthesis was performed using a dUTP-incorporation protocol to maintain strand specificity. The resulting double-stranded cDNA was end-repaired, A-tailed, and ligated to Illumina adapters, followed by size selection (250–300 bp insert) and PCR amplification. Libraries were quantified, quality-checked, and sequenced on an Illumina NovaSeq X Plus platform to generate paired-end 150 bp reads (PE150).

Bioinformatic analysis

All analyses were performed on the Galaxy platform unless otherwise stated. Raw reads were quality-trimmed with Trim Galore! to remove adapter sequences and low-quality bases.

RNA-seq

For RNA-seq, clean reads were aligned to the Mus musculus mm9 reference genome using HISAT2, and gene-level counts were obtained with featureCounts. Normalization and differential expression analysis were performed with DESeq2, using the median-of-ratios method. P-values were adjusted for multiple testing using the Benjamini–Hochberg procedure, and genes with adjusted $P < 0.05$ were considered significantly differentially expressed. Normalized counts generated by DESeq2 were extracted and used for downstream visualization. Volcano plots were generated by plotting the $\log_2$(fold change) against $-\log_{10}$(adjusted P-values) to highlight significantly upregulated and downregulated genes.

ChIP-seq

Trimmed reads were aligned to the Mus musculus mm9 reference genome with Bowtie2, then filtered with SAMtools to retain only properly paired reads with a mapping quality ≥ 30 while excluding mitochondrial reads (chrM). PCR and optical duplicates were removed with Picard MarkDuplicates, and only unique, high-quality reads were used in downstream analyses. Peaks were called with MACS2. Consensus peaks were defined as those present in both biological replicates using bedtools intersect. For each cell line, BRD2/BRD4 co-occupied regions were identified by intersecting BRD2 and BRD4 consensus peak sets. Regions were recentered on peak summits and extended ± 2 kb to create fixed windows for signal extraction. Signal coverage tracks were generated from duplicate-removed BAM files using deepTools bamCoverage with read-depth normalization. Signal changes across ranked regions were visualized with deepTools (plotHeatmap, plotProfile), confirming BRD4 loss and distinct BRD2 dynamics between sensitive and resistant cells. Per-region signal was extracted using deepTools computeMatrix reference-point (±2,000 bp, 50-bp bins, refPoint = center, skipZeros = true, missingDataAsZero = true). For each region, bins were averaged to obtain a single signal value per replicate and condition (DMSO, JQ1).

To quantify JQ1-sensitive BRD2 displacement, the difference was calculated for each region as $\Delta = BRD2_{DMSO} - BRD2_{JQ1}$. Replicate Δ values were averaged, and regions were ranked descending by Δ (larger positive Δ = stronger BRD2 loss after JQ1). The top 1,000 JQ1-sensitive BRD2 regions of mT3-2D (mm9 coordinates) were mapped to candidate genes using GREAT with the default basal-plus-extension model (proximal 5 kb upstream, 1 kb downstream, distal up to 1 Mb). This produced 1,208 non-redundant genes after excluding invalid identifiers. The set of 1,208 non-redundant genes identified from JQ1-sensitive BRD2 regions was analyzed for functional enrichment using ShinyGO (http://bioinformatics.sdstate.edu/go/). Input was provided as official *Mus musculus* gene IDs. Enrichment was performed against the default mouse genome background, restricted to GO Biological Process (GOBP) categories. Significance was determined using the Benjamini–Hochberg false discovery rate (FDR) correction, with terms at FDR $q < 0.05$ considered enriched. The top 20 enriched terms were reported. These 1,208 genes were cross-referenced with the RNA-seq expression matrix (DESeq2-normalized counts) for integrative analysis. The filtered gene set was imported into the Morpheus web tool (https://software.broadinstitute.org/morpheus) to generate clustered heatmaps of expression values. Genes were further ranked by the magnitude of expression loss in sensitive cells following JQ1, highlighting the most transcriptionally affected BRD2-associated targets.

Publicly available datasets

<u>RNA-seq analysis of BRD2 response to BET inhibition (JQ1)</u>

RNA-seq expression data from human conventional cancer cell lines were obtained via the GEO2R portal. Differential expression analysis was performed using DESeq2. Log_2fold change and adjusted p-values for *BRD2* were extracted to evaluate its response to JQ1 treatment, and these values were visualized as dot plots in R across multiple datasets. In addition, 3D volcano plots were generated in R using DESeq2 output to highlight differential expression patterns, with

a focus on both *BRD2* and *NFYA*. The individual datasets used in this analysis, including GEO accession numbers, cancer types, and sample information, are summarized in the table below.

Prostate cancer

GEO accession	Cancer type	Samples	References
GSE78213	Castrate-resistant prostate cancer	C4-2	(15)
GSE69896	Castrate-resistant prostate cancer	MR49F	(16)
GSE147876	Castrate-resistant prostate cancer	MR42D	(17)
GSE162564	Castrate-resistant prostate cancer	22RV-1	(18)
GSE126779	Castrate-resistant prostate cancer	DU145, PC3	(19)

Breast cancer

GEO accession	Cancer type	Samples	References
GSE171908	Triple-negative breast cancer	MCF-7, MDA-MB-231	(20)
GSE102407	Triple-negative breast cancer	MDA-MB-231	(21)
GSE219191	Triple-negative breast cancer	MDA-MB-231	(22)
GSE63582	Triple-negative breast cancer	SUM149, SUM159 (parental only)	(23)
GSE123285	Triple-negative breast cancer	MCF-7	(24)
GSE235201	Triple-negative breast cancer	HCC70, MDA-MB-231	(25)
GSE236250	Triple-negative breast cancer	MDA-MB-231	(26)
GSE115550	Triple-negative breast cancer	MDA-MB-231	
GSE116907	Triple-negative breast cancer	HCC1806, MDA-MB-231, SUM159	(27)
GSE109570	Luminal A breast cancer	MCF-7	(28)
GSE55922	Luminal A breast cancer	MCF-7	(29)
GSE114937	Breast cancer	MDA-MB-231, MDA-MB-453, SKBR3	(30)

Brain cancer

GEO accession	Cancer type	Samples	References
GSE99175	Glioblastoma	U-87 MG	(31)
GSE245006	Neuroblastoma	SK-N-BE(2)	(32)
GSE138942	Glioblastoma	U3009MG, U3024MG, U3054MG, U3056MG	(33)
GSE185024	Medulloblastoma	D425	(34)
GSE107707	Neuroblastoma	SK-N-BE(2)-C, Kelly (parental only)	(35)
GSE183587	Neuroblastoma	IMR-32	(36)

Skin cancer

GEO accession	Cancer type	Samples	References
GSE95153	Cutaneous melanoma	M93-047	(37)
GSE94488	Cutaneous melanoma	SKmel2, 501MEL, SKmel147	(38)
GSE131967	Squamous cell carcinoma	FaDu, SCC1, SCC22B	(39)

Gastrointestinal cancer

GEO accession	Cancer type	Samples	References
GSE95513	Colorectal cancer	RKO	(40)
GSE118548	Colorectal cancer	T84	(41)
GSE192903	Pancreatic cancer	PANC-1	(42)
GSE113215	Gastrointestinal stromal tumor	GIST-T1	(43)
GSE184065	Hepatocellular carcinoma	Huh7	(44)
GSE158552	Hepatocellular carcinoma	HepG2	(45)
GSE73318	Colorectal cancer	COLO205, COLO320, HCT116, HT-15, HT-29, SW480	(46)
GSE255300	Colorectal cancer	HCT116, HPCEC, HT29	(47)

Lung cancer

GEO accession	Cancer type	Samples	References
GSE210101	Small cell lung cancer	H446	(48)
GSE182821	Small cell lung cancer	NCI-H1688	(49)
GSE197426	Small cell lung cancer	NCI-H526	(50)
GSE113711	Non-small cell lung cancer	H23	(51)

Pediatric cancer

GEO accession	Cancer type	Samples	References
GSE145469	Rhabdomyosarcoma	Rh30	(52)
GSE196057	Atypical teratoid/rhabdoid tumor	BT12	(53)
GSE113604	Ewing sarcoma	Cado-ES, CHLA10, RD-ES, SK-N-MC	(54)

Gynecologic cancer

GEO accession	Cancer type	Samples	References
GSE235031	Ovarian cancer	A1847, A2780, OVCAR5	(55)
GSE82329	Cervical cancer	HeLa	(56)

Hematologic cancer

GEO accession	Cancer type	Samples	References
GSE188437	Multiple myeloma	OPM2	(57)
GSE79253	T-cell acute lymphoblastic leukemia	MOLT4	(58)
GSE77295	Chronic myelogenous leukemia	K562	(59)
GSE119744	Chronic lymphocytic leukemia	MEC1, MEC2, OSU-CKK, CII	(60)
GSE97435	T-cell acute lymphoblastic leukemia	Jurkat	(61)
GSE70447	Multiple myeloma	LP-1	
GSE92456	Burkitt's lymphoma	Raji	(62)
GSE129449	Acute myeloid leukemia	AML18	(63)

<u>RNA-seq analysis of BRD4 knockdown</u>

RNA-seq data from human conventional cancer cell lines were obtained from the GEO2R portal. Normalized counts were extracted as provided, and BRD2 expression was compared between control and BRD4 knockdown conditions. Statistical significance was assessed using a two-tailed Student's t-test, and results were visualized in Prism.

GEO accession	Cancer type	Samples	References
GSE215393	Rhabdomyosarcoma	RD	(65)
GSE50491	Human embryonic kidney	HEK293T	(66)
GSE73317	Liver cancer	HCT116, HT-29	(46)
GSE206667	Breast cancer	MCF-7	(67)
GSE90444	Pancreatic cancer	KP-4	(68)
GSE113604	Ewing sarcoma	Cado-ES, CHLA10, RD-ES, SK-N-MC	(54)

ChIP-seq

BRD2 and BRD4 ChIP-seq data from human breast cancer cell lines (GSE131907) were obtained from GEO. Processed peak files (BED) and signal tracks (bigWig) were used directly. Binding sites were intersected using bedtools intersect to define co-occupied regions, and signal distribution across these regions was assessed with deepTools (computeMatrix) followed by plotProfile to generate meta-profiles. All analyses were performed on the Galaxy platform.

BRD2 and BRD4 ChIP-seq

GEO accession	Cancer type	Samples	References
GSE131097	Triple-negative breast cancer	SUM149	(69)

NFYA ChIP-seq

GEO accession	Cancer type	Samples	References
GSE31477 (GSM935433)	Chronic myelogenous leukemia	K562	(77)
GSE31477 (GSM935508)	Cervical cancer	HeLa-S3	(77)
GSE31477 (GSM935506)	Lymphoblastoid cells	GM12878	(77)
GSE51142	Colorectal cancer	LoVo	(78)

Statistical analysis

All statistical analyses were performed using GraphPad Prism 10. Statistical significance between two groups was assessed using a two-tailed unpaired Student's t-test. For comparisons involving

more than two groups, one-way ANOVA followed by multiple comparisons testing was applied. A p-value < 0.05 was considered statistically significant. Error bars represent the SEM unless otherwise indicated.

Data availability

Raw and processed RNA-seq and ChIP-seq data will be deposited in the GEO.

ACKNOWLEDGEMENTS

This study was supported by National Cancer Institute grant 5R37CA249007 (C.-I.H). The authors would like to thank all members of the Hwang lab for their support throughout the course of this study, particularly Jihao Xu and Mihn Duc Pham for their helpful discussions. S.A. was supported by the Anandamahidol Foundation and University of California Davis Comprehensive Cancer Center Director’s Fellowship. J.J. was supported by Provost's Undergraduate Fellowship.

REFERENCES

1. Hanahan D, Weinberg RA. Hallmarks of cancer: the next generation. Cell **2011**;144:646–74
2. Hanahan D. Hallmarks of Cancer: New Dimensions. Cancer Discov **2022**;12:31–46
3. Bradner JE, Hnisz D, Young RA. Transcriptional Addiction in Cancer. Cell **2017**;168:629–43
4. Shi J, Vakoc CR. The mechanisms behind the therapeutic activity of BET bromodomain inhibition. Mol Cell **2014**;54:728–36
5. Dhalluin C, Carlson JE, Zeng L, He C, Aggarwal AK, Zhou MM. Structure and ligand of a histone acetyltransferase bromodomain. Nature **1999**;399:491–6
6. Loven J, Hoke HA, Lin CY, Lau A, Orlando DA, Vakoc CR*, et al.* Selective inhibition of tumor oncogenes by disruption of super-enhancers. Cell **2013**;153:320–34
7. Jang MK, Mochizuki K, Zhou M, Jeong HS, Brady JN, Ozato K. The bromodomain protein Brd4 is a positive regulatory component of P-TEFb and stimulates RNA polymerase II-dependent transcription. Mol Cell **2005**;19:523–34
8. Filippakopoulos P, Qi J, Picaud S, Shen Y, Smith WB, Fedorov O*, et al.* Selective inhibition of BET bromodomains. Nature **2010**;468:1067–73
9. Zuber J, Shi J, Wang E, Rappaport AR, Herrmann H, Sison EA*, et al.* RNAi screen identifies Brd4 as a therapeutic target in acute myeloid leukaemia. Nature **2011**;478:524–8
10. Delmore JE, Issa GC, Lemieux ME, Rahl PB, Shi J, Jacobs HM*, et al.* BET bromodomain inhibition as a therapeutic strategy to target c-Myc. Cell **2011**;146:904–17
11. Roe JS, Mercan F, Rivera K, Pappin DJ, Vakoc CR. BET Bromodomain Inhibition Suppresses the Function of Hematopoietic Transcription Factors in Acute Myeloid Leukemia. Mol Cell **2015**;58:1028–39
12. Berthon C, Raffoux E, Thomas X, Vey N, Gomez-Roca C, Yee K*, et al.* Bromodomain inhibitor OTX015 in patients with acute leukaemia: a dose-escalation, phase 1 study. Lancet Haematol **2016**;3:e186–95
13. Braun T, Gardin C. Investigational BET bromodomain protein inhibitors in early stage clinical trials for acute myelogenous leukemia (AML). Expert Opin Investig Drugs **2017**;26:803–11
14. Khandekar D, Tiriveedhi V. Role of BET Inhibitors in Triple Negative Breast Cancers. Cancers (Basel) **2020**;12
15. Zhang P, Wang D, Zhao Y, Ren S, Gao K, Ye Z*, et al.* Intrinsic BET inhibitor resistance in SPOP-mutated prostate cancer is mediated by BET protein stabilization and AKT-mTORC1 activation. Nat Med **2017**;23:1055–62
16. Coleman DJ, Van Hook K, King CJ, Schwartzman J, Lisac R, Urrutia J*, et al.* Cellular androgen content influences enzalutamide agonism of F877L mutant androgen receptor. Oncotarget **2016**;7:40690–703
17. Kim DH, Sun D, Storck WK, Welker Leng K, Jenkins C, Coleman DJ*, et al.* BET Bromodomain Inhibition Blocks an AR-Repressed, E2F1-Activated Treatment-Emergent Neuroendocrine Prostate Cancer Lineage Plasticity Program. Clin Cancer Res **2021**;27:4923–36
18. Welti J, Sharp A, Brooks N, Yuan W, McNair C, Chand SN*, et al.* Targeting the p300/CBP Axis in Lethal Prostate Cancer. Cancer Discov **2021**;11:1118–37

19. Mao W, Ghasemzadeh A, Freeman ZT, Obradovic A, Chaimowitz MG, Nirschl TR*, et al.* Immunogenicity of prostate cancer is augmented by BET bromodomain inhibition. J Immunother Cancer **2019**;7:277
20. Liu B, Liu X, Han L, Chen X, Wu X, Wu J*, et al.* BRD4-directed super-enhancer organization of transcription repression programs links to chemotherapeutic efficacy in breast cancer. Proc Natl Acad Sci U S A **2022**;119
21. Zanconato F, Battilana G, Forcato M, Filippi L, Azzolin L, Manfrin A*, et al.* Transcriptional addiction in cancer cells is mediated by YAP/TAZ through BRD4. Nat Med **2018**;24:1599–610
22. Lu X, Peng L, Ding J, Li Y, Li Q, Rao M*, et al.* A deregulated m(6)A writer complex axis driven by BRD4 confers an epitranscriptomic vulnerability in combined DNA repair-targeted therapy. Proc Natl Acad Sci U S A **2023**;120:e2304534120
23. Shu S, Lin CY, He HH, Witwicki RM, Tabassum DP, Roberts JM*, et al.* Response and resistance to BET bromodomain inhibitors in triple-negative breast cancer. Nature **2016**;529:413–7
24. Nagarajan S, Rao SV, Sutton J, Cheeseman D, Dunn S, Papachristou EK*, et al.* ARID1A influences HDAC1/BRD4 activity, intrinsic proliferative capacity and breast cancer treatment response. Nat Genet **2020**;52:187–97
25. Vinik Y, Maimon A, Raj H, Dubey V, Geist F, Wienke D*, et al.* Computational pipeline predicting cell death suppressors as targets for cancer therapy. iScience **2024**;27:110859
26. Bevill SM, Olivares-Quintero JF, Sciaky N, Golitz BT, Singh D, Beltran AS*, et al.* GSK2801, a BAZ2/BRD9 Bromodomain Inhibitor, Synergizes with BET Inhibitors to Induce Apoptosis in Triple-Negative Breast Cancer. Mol Cancer Res **2019**;17:1503–18
27. Ren C, Zhang G, Han F, Fu S, Cao Y, Zhang F*, et al.* Spatially constrained tandem bromodomain inhibition bolsters sustained repression of BRD4 transcriptional activity for TNBC cell growth. Proc Natl Acad Sci U S A **2018**;115:7949–54
28. Murakami S, Li R, Nagari A, Chae M, Camacho CV, Kraus WL. Distinct Roles for BET Family Members in Estrogen Receptor alpha Enhancer Function and Gene Regulation in Breast Cancer Cells. Mol Cancer Res **2019**;17:2356–68
29. Nagarajan S, Hossan T, Alawi M, Najafova Z, Indenbirken D, Bedi U*, et al.* Bromodomain protein BRD4 is required for estrogen receptor-dependent enhancer activation and gene transcription. Cell Rep **2014**;8:460–9
30. Garcia-Carpizo V, Ruiz-Llorente S, Sarmentero J, Gonzalez-Corpas A, Barrero MJ. CREBBP/EP300 Bromodomain Inhibition Affects the Proliferation of AR-Positive Breast Cancer Cell Lines. Mol Cancer Res **2019**;17:720–30
31. Xu L, Chen Y, Mayakonda A, Koh L, Chong YK, Buckley DL*, et al.* Targetable BET proteins- and E2F1-dependent transcriptional program maintains the malignancy of glioblastoma. Proc Natl Acad Sci U S A **2018**;115:E5086–E95
32. Stokes ME, Vasciaveo A, Small JC, Zask A, Reznik E, Smith N*, et al.* Subtype-selective prenylated isoflavonoids disrupt regulatory drivers of MYCN-amplified cancers. Cell Chem Biol **2024**;31:805–19 e9
33. Cancer M, Drews LF, Bengtsson J, Bolin S, Rosen G, Westermark B*, et al.* BET and Aurora Kinase A inhibitors synergize against MYCN-positive human glioblastoma cells. Cell Death Dis **2019**;10:881
34. Li M, Han Y, Wang C, Kang W, Jiang W, Zhang L*, et al.* Dissecting super-enhancer driven transcriptional dependencies reveals novel therapeutic strategies and targets for group 3 subtype medulloblastoma. J Exp Clin Cancer Res **2022**;41:311
35. Iniguez AB, Alexe G, Wang EJ, Roti G, Patel S, Chen L*, et al.* Resistance to Epigenetic-Targeted Therapy Engenders Tumor Cell Vulnerabilities Associated with Enhancer Remodeling. Cancer Cell **2018**;34:922–38 e7

36. Gao Y, Volegova M, Nasholm N, Das S, Kwiatkowski N, Abraham BJ*, et al.* Synergistic Anti-Tumor Effect of Combining Selective CDK7 and BRD4 Inhibition in Neuroblastoma. Front Oncol **2021**;11:773186
37. Echevarria-Vargas IM, Reyes-Uribe PI, Guterres AN, Yin X, Kossenkov AV, Liu Q*, et al.* Co-targeting BET and MEK as salvage therapy for MAPK and checkpoint inhibitor-resistant melanoma. EMBO Mol Med **2018**;10
38. Fontanals-Cirera B, Hasson D, Vardabasso C, Di Micco R, Agrawal P, Chowdhury A*, et al.* Harnessing BET Inhibitor Sensitivity Reveals AMIGO2 as a Melanoma Survival Gene. Mol Cell **2017**;68:731–44 e9
39. Dong J, Li J, Li Y, Ma Z, Yu Y, Wang CY. Transcriptional super-enhancers control cancer stemness and metastasis genes in squamous cell carcinoma. Nat Commun **2021**;12:3974
40. Wu T, Wang G, Chen W, Zhu Z, Liu Y, Huang Z*, et al.* Co-inhibition of BET proteins and NF-kappaB as a potential therapy for colorectal cancer through synergistic inhibiting MYC and FOXM1 expressions. Cell Death Dis **2018**;9:315
41. Wagner S, Vlachogiannis G, De Haven Brandon A, Valenti M, Box G, Jenkins L*, et al.* Suppression of interferon gene expression overcomes resistance to MEK inhibition in KRAS-mutant colorectal cancer. Oncogene **2019**;38:1717–33
42. Principe DR, Xiong R, Li Y, Pham TND, Kamath SD, Dubrovskyi O*, et al.* XP-524 is a dual-BET/EP300 inhibitor that represses oncogenic KRAS and potentiates immune checkpoint inhibition in pancreatic cancer. Proc Natl Acad Sci U S A **2022**;119
43. Hemming ML, Lawlor MA, Andersen JL, Hagan T, Chipashvili O, Scott TG*, et al.* Enhancer Domains in Gastrointestinal Stromal Tumor Regulate KIT Expression and Are Targetable by BET Bromodomain Inhibition. Cancer Res **2019**;79:994–1009
44. Li F, Liu P, Mi W, Li L, Anderson NM, Lesner NP*, et al.* Blocking methionine catabolism induces senescence and confers vulnerability to GSK3 inhibition in liver cancer. Nat Cancer **2024**;5:131–46
45. Baek M, Chai JC, Choi HI, Yoo E, Binas B, Lee YS*, et al.* Comprehensive transcriptome profiling of BET inhibitor-treated HepG2 cells. PLoS One **2022**;17:e0266966
46. McCleland ML, Mesh K, Lorenzana E, Chopra VS, Segal E, Watanabe C*, et al.* CCAT1 is an enhancer-templated RNA that predicts BET sensitivity in colorectal cancer. J Clin Invest **2016**;126:639–52
47. Zhu Y, Lee H, White S, Weimer AK, Monte E, Horning A*, et al.* Global loss of promoter-enhancer connectivity and rebalancing of gene expression during early colorectal cancer carcinogenesis. Nat Cancer **2024**;5:1697–712
48. Chen H, Gesumaria L, Park YK, Oliver TG, Singer DS, Ge K*, et al.* BET Inhibitors Target the SCLC-N Subtype of Small-Cell Lung Cancer by Blocking NEUROD1 Transactivation. Mol Cancer Res **2023**;21:91–101
49. Zhong M, Li X, Zhao F, Huang Y, Long Y, Chen K*, et al.* Natural compound library screening identifies Sanguinarine chloride for the treatment of SCLC by upregulating CDKN1A. Transl Oncol **2022**;17:101345
50. Szczepanski A, Tsuboyama N, Lyu H, Wang P, Beytullahoglu O, Zhang T*, et al.* A SWI/SNF-dependent transcriptional regulation mediated by POU2AF2/C11orf53 at enhancer. Nat Commun **2024**;15:2067
51. Handoko L, Kaczkowski B, Hon CC, Lizio M, Wakamori M, Matsuda T*, et al.* JQ1 affects BRD2-dependent and independent transcription regulation without disrupting H4-hyperacetylated chromatin states. Epigenetics **2018**;13:410–31
52. Boedicker C, Hussong M, Grimm C, Dolgikh N, Meister MT, Enssle JC*, et al.* Co-inhibition of BET proteins and PI3Kalpha triggers mitochondrial apoptosis in rhabdomyosarcoma cells. Oncogene **2020**;39:3837–52

53. Ishi Y, Zhang Y, Zhang A, Sasaki T, Piunti A, Suri A*, et al.* Therapeutic Targeting of EZH2 and BET BRD4 in Pediatric Rhabdoid Tumors. Mol Cancer Ther **2022**;21:715–26
54. Gollavilli PN, Pawar A, Wilder-Romans K, Natesan R, Engelke CG, Dommeti VL*, et al.* EWS/ETS-Driven Ewing Sarcoma Requires BET Bromodomain Proteins. Cancer Res **2018**;78:4760–73
55. Kurimchak AM, Shelton C, Duncan KE, Johnson KJ, Brown J, O'Brien S*, et al.* Resistance to BET Bromodomain Inhibitors Is Mediated by Kinome Reprogramming in Ovarian Cancer. Cell Rep **2016**;16:1273–86
56. Zheng J, Huang B, Xiao L, Wu M. Effects of BRD4 inhibitor JQ1 on the expression profile of super-enhancer related lncRNAs and mRNAs in cervical cancer HeLa cells. PeerJ **2024**;12:e17035
57. Oh DH, Ma X, Hogg SJ, He J, Kearney C, Brasacchio D*, et al.* Rationally designed chimeric PI3K-BET bromodomain inhibitors elicit curative responses in MYC-driven lymphoma. Proc Natl Acad Sci U S A **2023**;120:e2306414120
58. Winter GE, Mayer A, Buckley DL, Erb MA, Roderick JE, Vittori S*, et al.* BET Bromodomain Proteins Function as Master Transcription Elongation Factors Independent of CDK9 Recruitment. Mol Cell **2017**;67:5–18 e9
59. Garcia-Carpizo V, Ruiz-Llorente S, Sarmentero J, Grana-Castro O, Pisano DG, Barrero MJ. CREBBP/EP300 bromodomains are critical to sustain the GATA1/MYC regulatory axis in proliferation. Epigenetics Chromatin **2018**;11:30
60. Ott CJ, Federation AJ, Schwartz LS, Kasar S, Klitgaard JL, Lenci R*, et al.* Enhancer Architecture and Essential Core Regulatory Circuitry of Chronic Lymphocytic Leukemia. Cancer Cell **2018**;34:982–95 e7
61. Jin Q, Martinez CA, Arcipowski KM, Zhu Y, Gutierrez-Diaz BT, Wang KK*, et al.* USP7 Cooperates with NOTCH1 to Drive the Oncogenic Transcriptional Program in T-Cell Leukemia. Clin Cancer Res **2019**;25:222–39
62. Decker TM, Kluge M, Krebs S, Shah N, Blum H, Friedel CC*, et al.* Transcriptome analysis of dominant-negative Brd4 mutants identifies Brd4-specific target genes of small molecule inhibitor JQ1. Sci Rep **2017**;7:1684
63. McCalmont H, Li KL, Jones L, Toubia J, Bray SC, Casolari DA*, et al.* Efficacy of combined CDK9/BET inhibition in preclinical models of MLL-rearranged acute leukemia. Blood Adv **2020**;4:296–300
64. Lee E, Archasappawat S, Ji K, Pena J, Fernandez-Vega V, Gangaraju R*, et al.* A new vulnerability to BET inhibition due to enhanced autophagy in BRCA2 deficient pancreatic cancer. Cell Death Dis **2023**;14:620
65. Das D, Leung JY, Balamurugan S, Tergaonkar V, Loh AHP, Chiang CM*, et al.* BRD4 isoforms have distinct roles in tumour progression and metastasis in rhabdomyosarcoma. EMBO Rep **2024**;25:832–52
66. Hussong M, Borno ST, Kerick M, Wunderlich A, Franz A, Sultmann H*, et al.* The bromodomain protein BRD4 regulates the KEAP1/NRF2-dependent oxidative stress response. Cell Death Dis **2014**;5:e1195
67. Liu L, Lin B, Yin S, Ball LE, Delaney JR, Long DT*, et al.* Arginine methylation of BRD4 by PRMT2/4 governs transcription and DNA repair. Sci Adv **2022**;8:eadd8928
68. Sakamaki JI, Wilkinson S, Hahn M, Tasdemir N, O'Prey J, Clark W*, et al.* Bromodomain Protein BRD4 Is a Transcriptional Repressor of Autophagy and Lysosomal Function. Mol Cell **2017**;66:517–32 e9
69. Shu S, Wu HJ, Ge JY, Zeid R, Harris IS, Jovanovic B*, et al.* Synthetic Lethal and Resistance Interactions with BET Bromodomain Inhibitors in Triple-Negative Breast Cancer. Mol Cell **2020**;78:1096–113 e8

70. Ito T, Young MJ, Li R, Jain S, Wernitznig A, Krill-Burger JM*, et al.* Paralog knockout profiling identifies DUSP4 and DUSP6 as a digenic dependence in MAPK pathway-driven cancers. Nat Genet **2021**;53:1664–72
71. Shinohara H, Sawado R, Nakagawa M, Hattori A, Yamagata K, Tauchi K*, et al.* Dual targeting of EZH1 and EZH2 for the treatment of malignant rhabdoid tumors. Mol Ther Oncolytics **2022**;27:14–25
72. Patel PO, Pishas KI, Taslim C, Selich-Anderson J, Theisen ER, Lessnick SL. Investigating the role of LSD2 as an epigenetic regulator in Ewing sarcoma. Oncotarget **2019**;10:3865–78
73. Hsu SC, Gilgenast TG, Bartman CR, Edwards CR, Stonestrom AJ, Huang P*, et al.* The BET Protein BRD2 Cooperates with CTCF to Enforce Transcriptional and Architectural Boundaries. Mol Cell **2017**;66:102–16 e7
74. Xie L, Dong P, Qi Y, Hsieh TS, English BP, Jung S*, et al.* BRD2 compartmentalizes the accessible genome. Nat Genet **2022**;54:481–91
75. Saenz DT, Fiskus W, Qian Y, Manshouri T, Rajapakshe K, Raina K*, et al.* Novel BET protein proteolysis-targeting chimera exerts superior lethal activity than bromodomain inhibitor (BETi) against post-myeloproliferative neoplasm secondary (s) AML cells. Leukemia **2017**;31:1951–61
76. Boj SF, Hwang CI, Baker LA, Chio, II, Engle DD, Corbo V*, et al.* Organoid models of human and mouse ductal pancreatic cancer. Cell **2015**;160:324–38
77. Pope BD, Ryba T, Dileep V, Yue F, Wu W, Denas O*, et al.* Topologically associating domains are stable units of replication-timing regulation. Nature **2014**;515:402–5
78. Yan J, Enge M, Whitington T, Dave K, Liu J, Sur I*, et al.* Transcription factor binding in human cells occurs in dense clusters formed around cohesin anchor sites. Cell **2013**;154:801–13

Figure 1

A Pan-cancer *BRD2* expression in response to JQ1

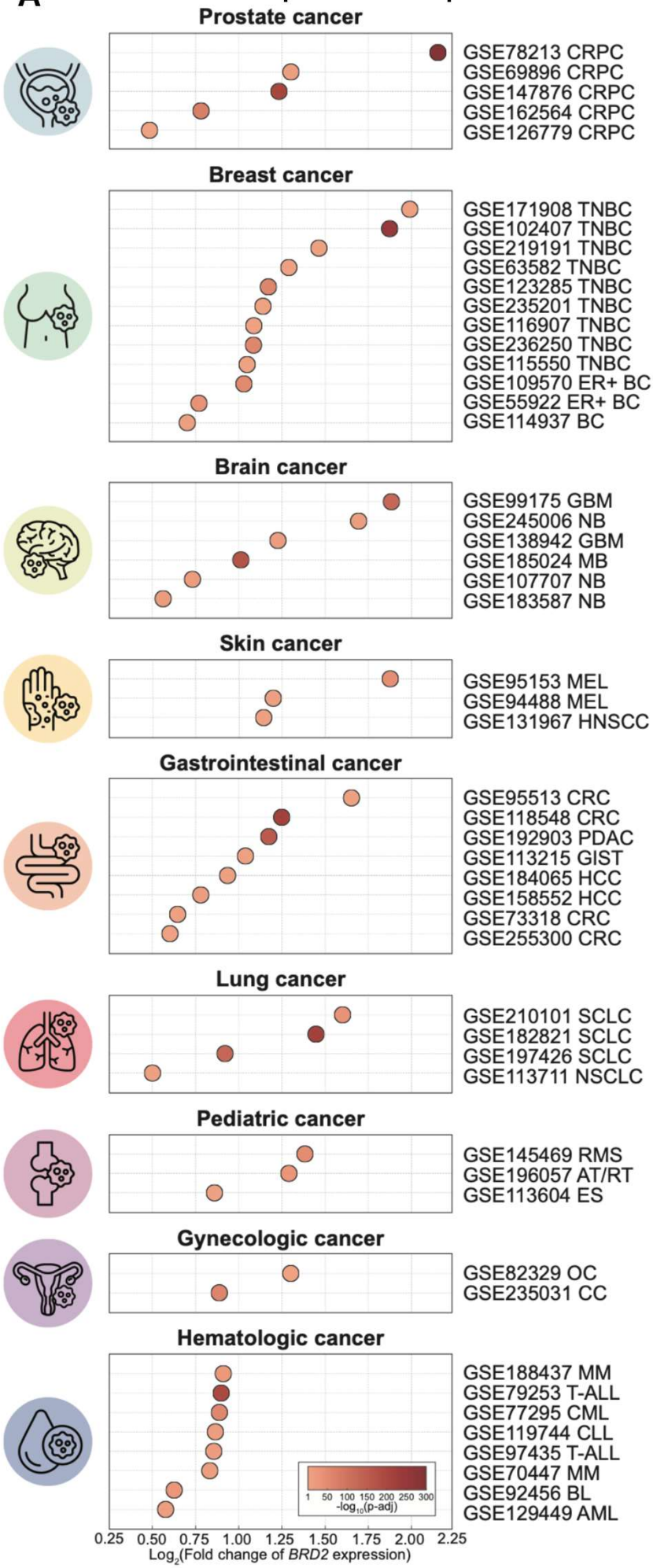

B

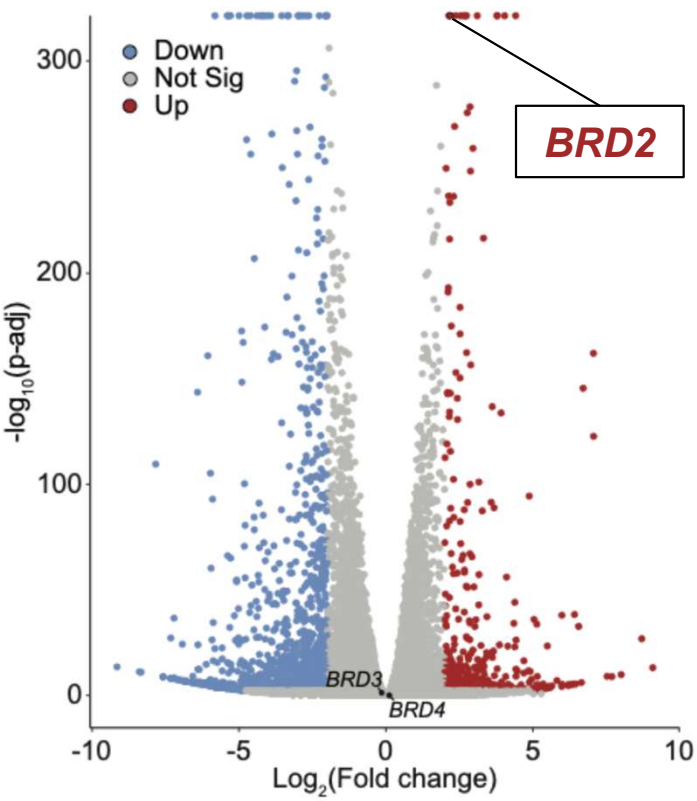

C

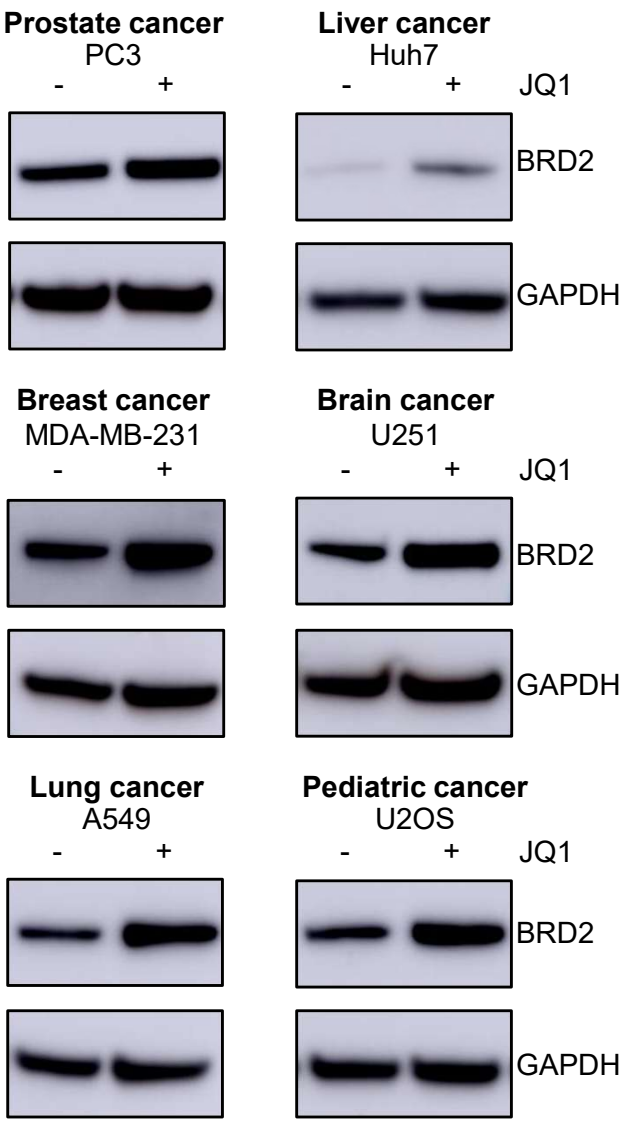

Figure 2

A

GSE192903
Differentially expressed genes
JQ1 vs. DMSO in human PDAC (PANC-1)

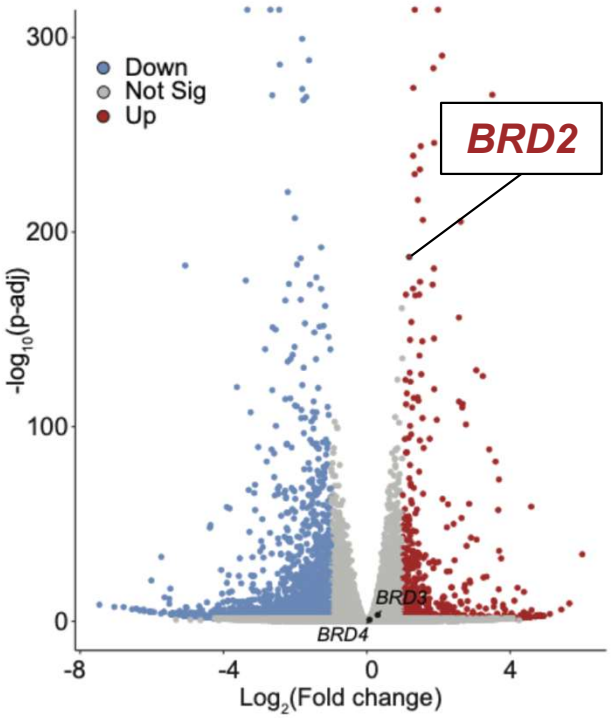

B

RNA-seq
Differentially expressed genes
JQ1 vs. DMSO in mouse PDAC
(mT3-2D, mT19-2D, mT23-2D)

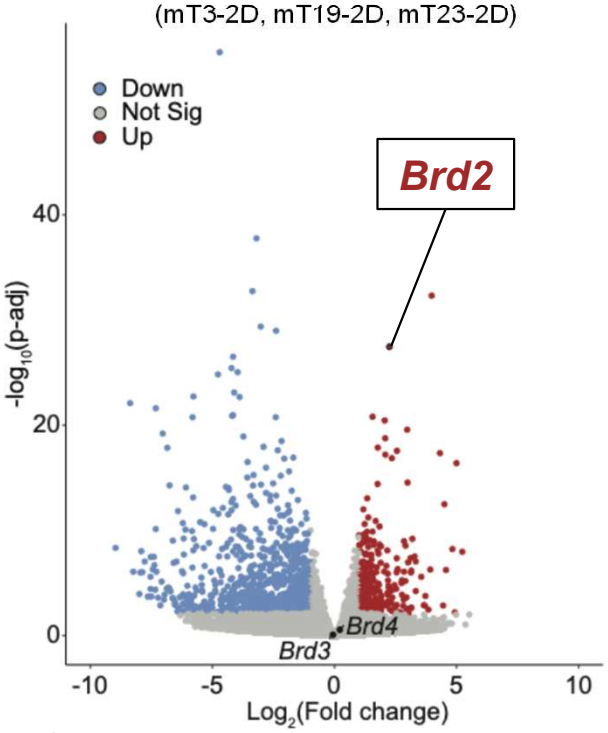

C

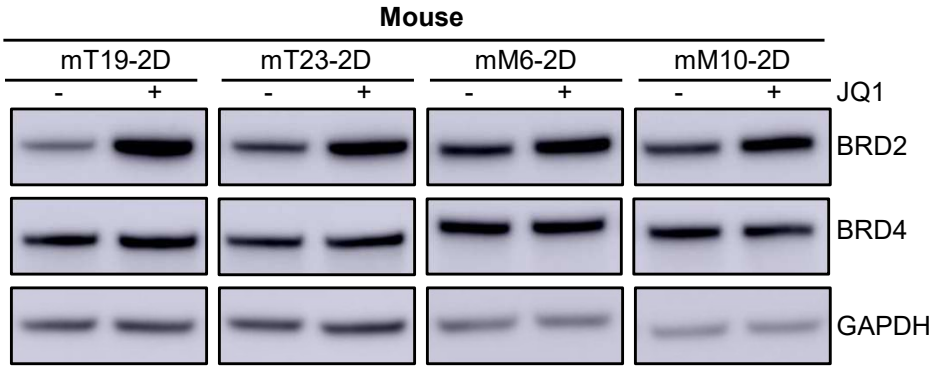

D

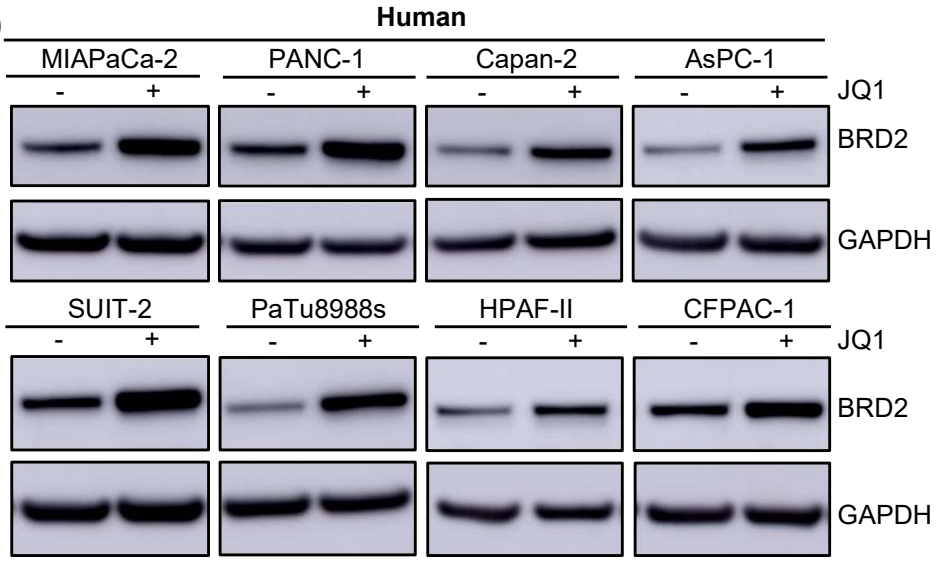

E

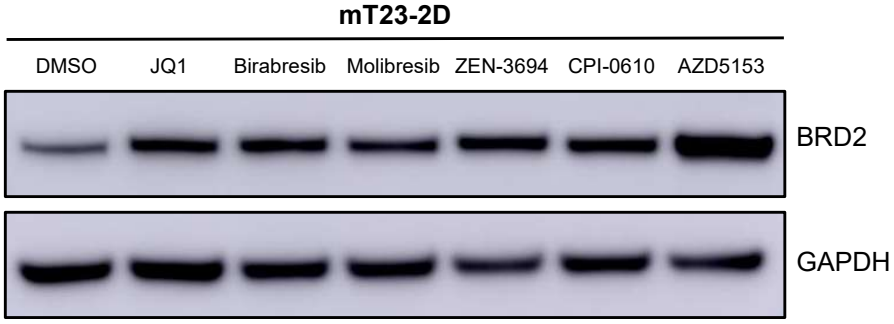

F

G

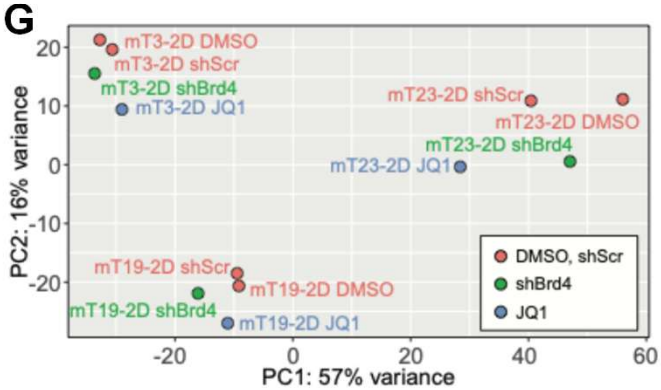

Figure 3

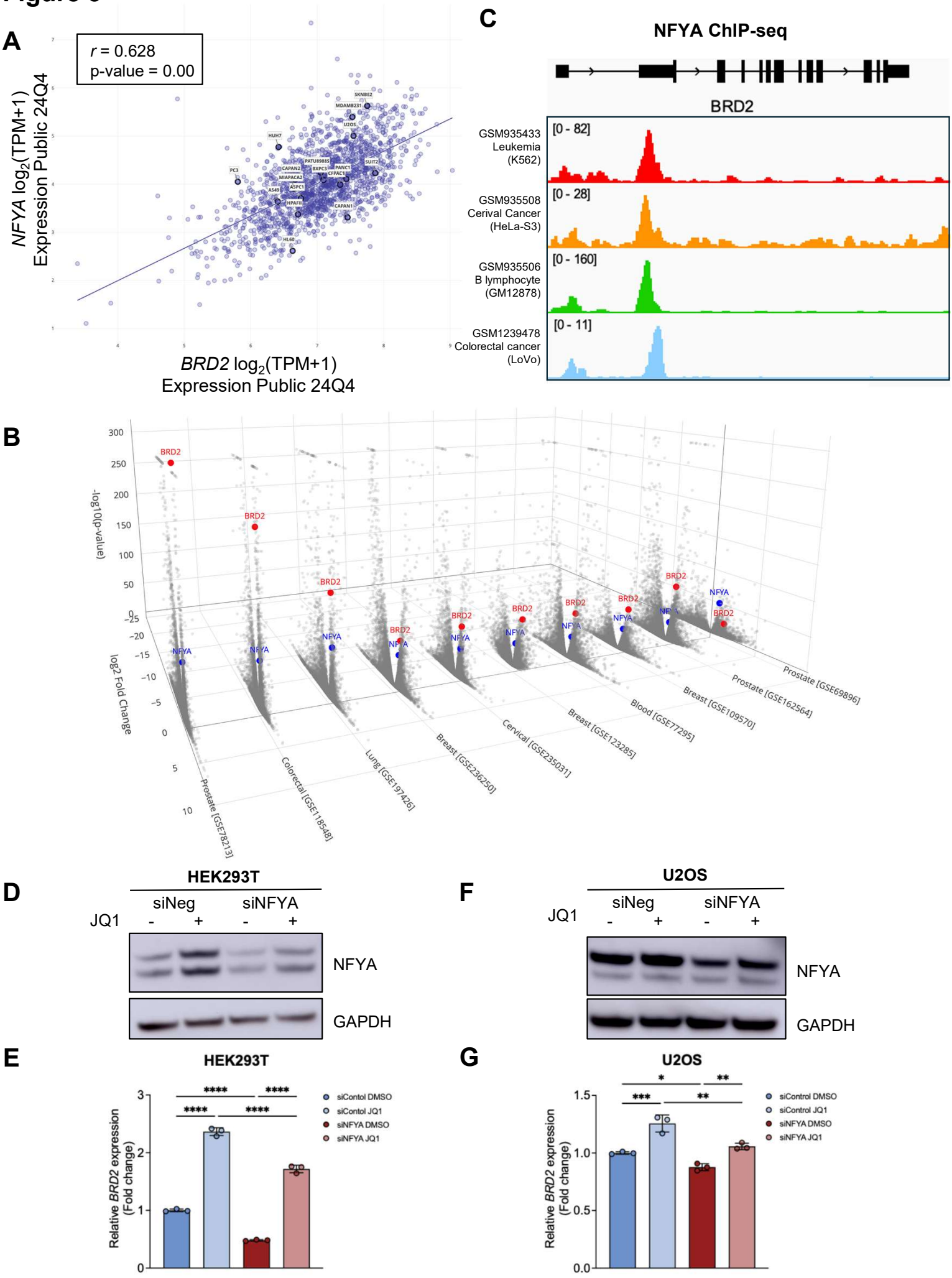
A
r = 0.628
p-value = 0.00
NFYA log2(TPM+1) Expression Public 24Q4
BRD2 log2(TPM+1) Expression Public 24Q4
C
NFYA ChIP-seq
BRD2
GSM935433 Leukemia (K562)
[0 - 82]
GSM935508 Cerival Cancer (HeLa-S3)
[0 - 28]
GSM935506 B lymphocyte (GM12878)
[0 - 160]
GSM1239478 Colorectal cancer (LoVo)
[0 - 11]
B
-log10(p-value)
log2 Fold Change
BRD2
NFYA
Prostate [GSE78213]
Colorectal [GSE118548]
Lung [GSE197426]
Breast [GSE236250]
Cervical [GSE235031]
Breast [GSE123285]
Blood [GSE77295]
Breast [GSE109570]
Prostate [GSE162564]
Prostate [GSE69896]
D
HEK293T
siNeg
siNFYA
JQ1
NFYA
GAPDH
F
U2OS
siNeg
siNFYA
JQ1
NFYA
GAPDH
E
HEK293T
Relative BRD2 expression (Fold change)
siContol DMSO
siContol JQ1
siNFYA DMSO
siNFYA JQ1
G
U2OS
Relative BRD2 expression (Fold change)
siControl DMSO
siControl JQ1
siNFYA DMSO
siNFYA JQ1

Figure 4

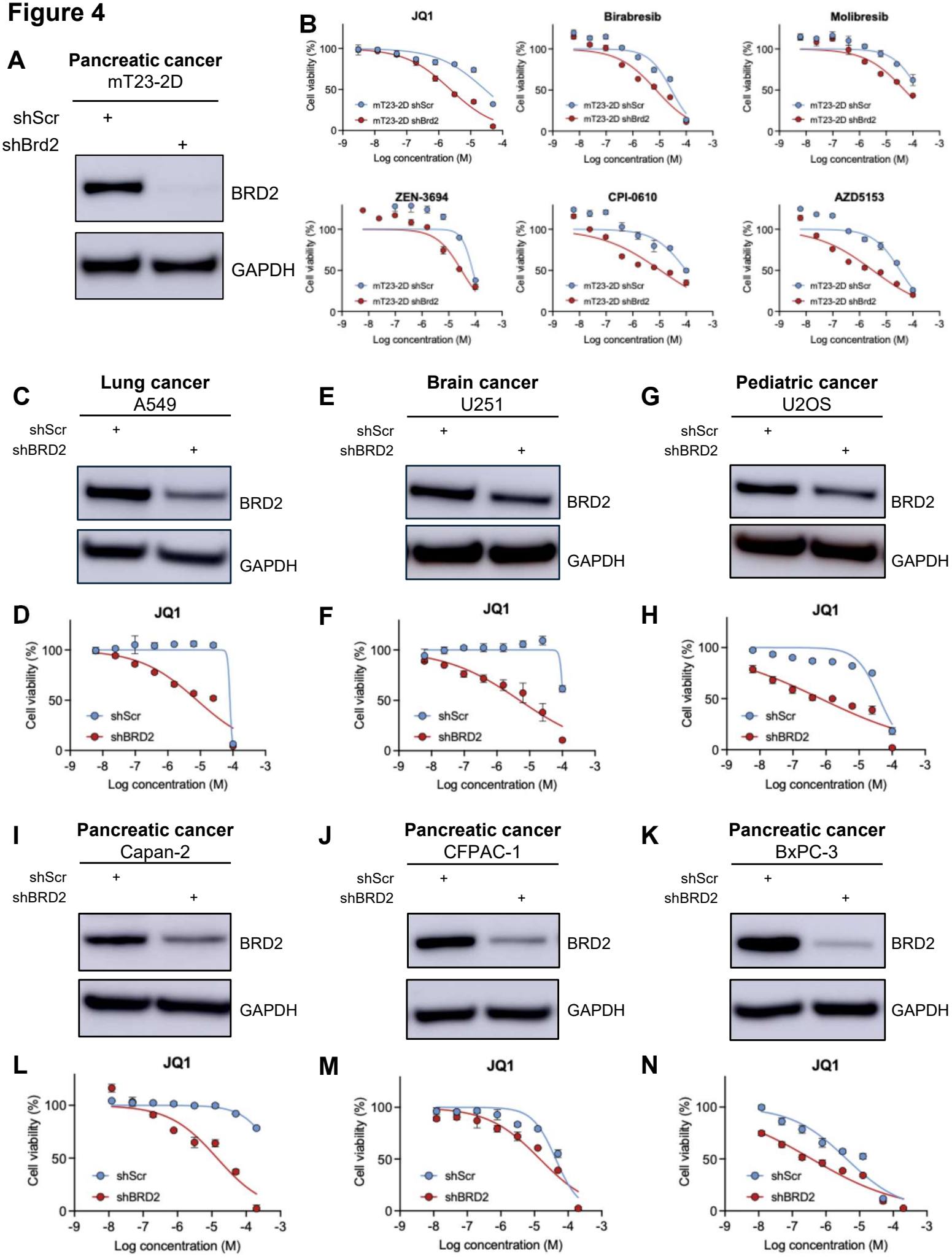
A
Pancreatic cancer
mT23-2D
shScr +
shBrd2 +
BRD2
GAPDH
B
JQ1
Birabresib
Molibresib
ZEN-3694
CPI-0610
AZD5153
Cell viability (%)
Log concentration (M)
mT23-2D shScr
mT23-2D shBrd2
C
Lung cancer
A549
E
Brain cancer
U251
G
Pediatric cancer
U2OS
shScr +
shBRD2 +
BRD2
GAPDH
D
F
H
JQ1
shScr
shBRD2
I
Pancreatic cancer
Capan-2
J
Pancreatic cancer
CFPAC-1
K
Pancreatic cancer
BxPC-3
L
M
N

Figure 5

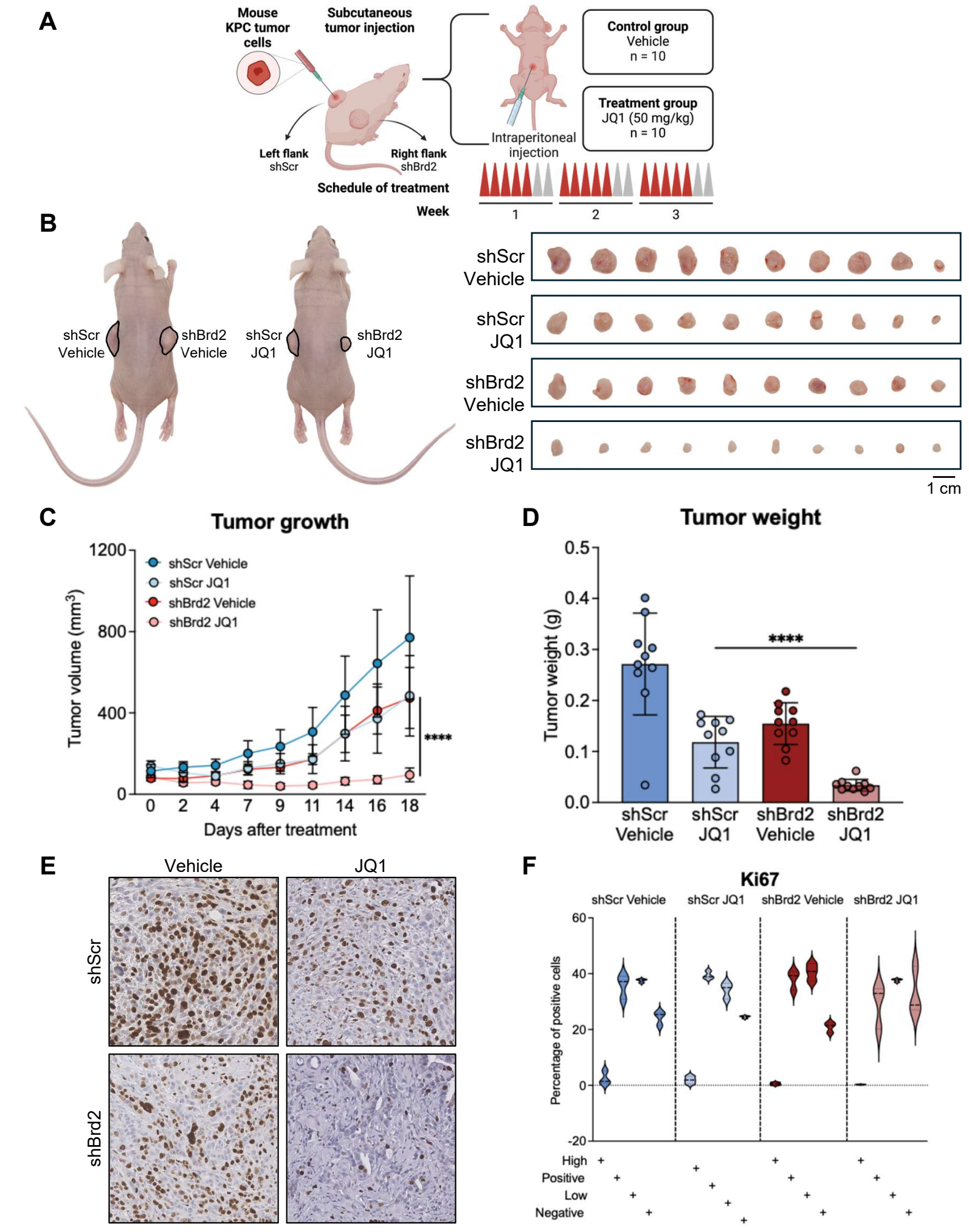
A
Mouse KPC tumor cells
Subcutaneous tumor injection
Left flank shScr
Right flank shBrd2
Intraperitoneal injection
Control group Vehicle n = 10
Treatment group JQ1 (50 mg/kg) n = 10
Schedule of treatment
Week
1
2
3
B
shScr Vehicle
shBrd2 Vehicle
shScr JQ1
shBrd2 JQ1
1 cm
C
Tumor growth
Tumor volume (mm³)
Days after treatment
shScr Vehicle
shScr JQ1
shBrd2 Vehicle
shBrd2 JQ1
****
D
Tumor weight
Tumor weight (g)
****
E
Vehicle
JQ1
shScr
shBrd2
F
Ki67
Percentage of positive cells
High
Positive
Low
Negative

Figure 6

A

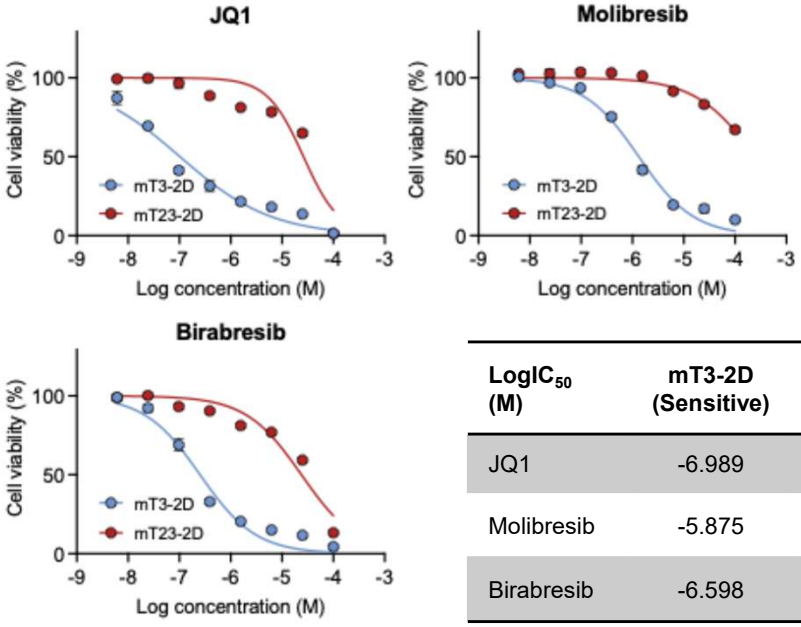

LogIC$_{50}$ (M)	mT3-2D (Sensitive)	mT23-2D (Resistant)
JQ1	-6.989	-4.583
Molibresib	-5.875	-0.7398
Birabresib	-6.598	-4.623

B

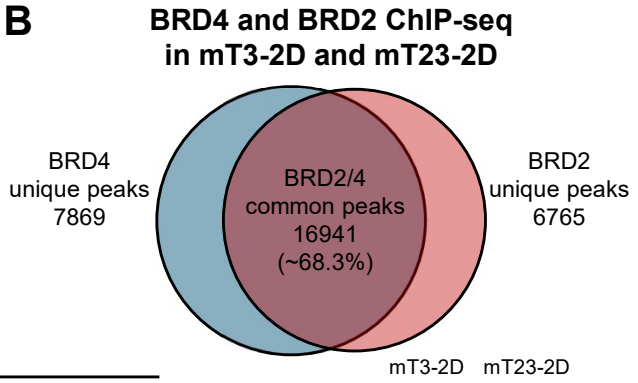

C

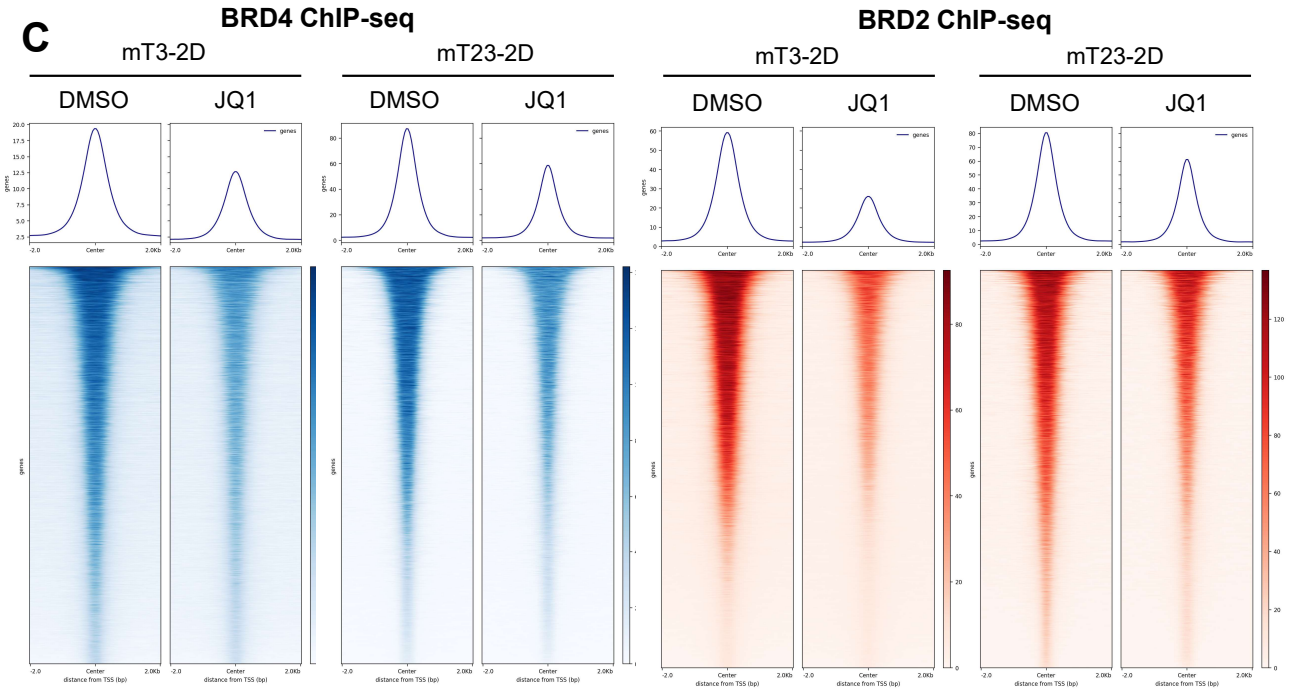

D

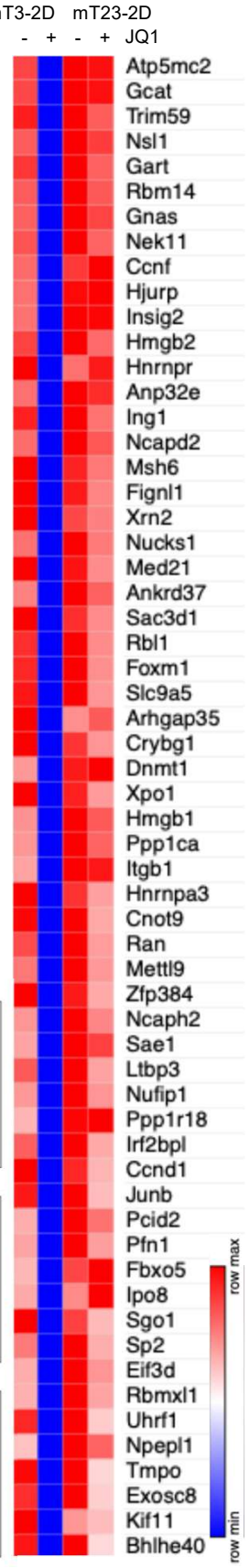

E

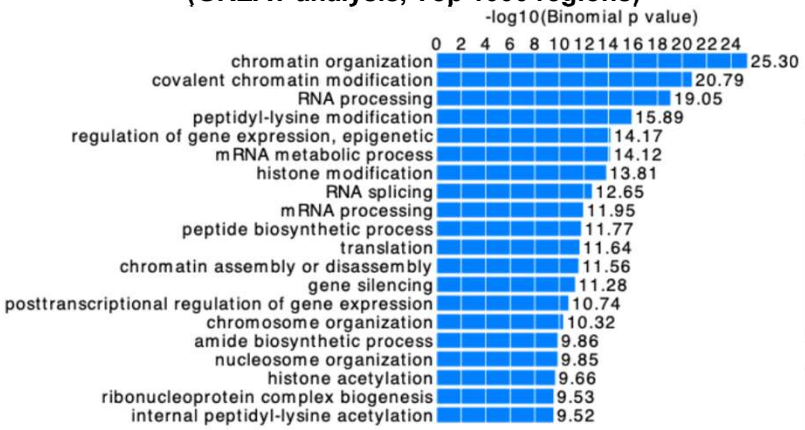

F

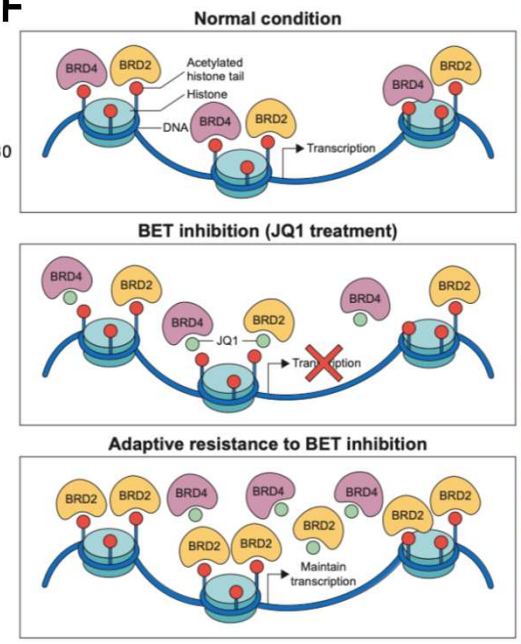

Supplementary Figure 1

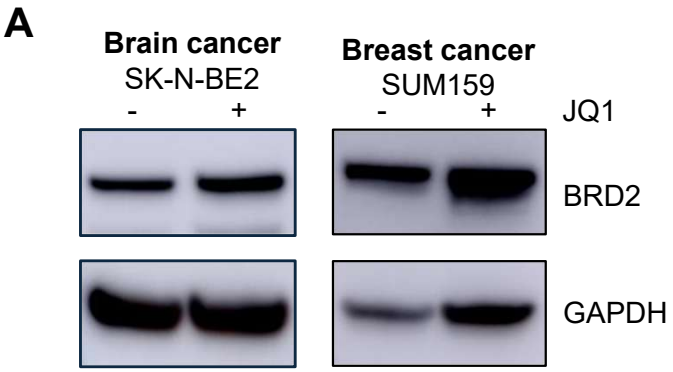

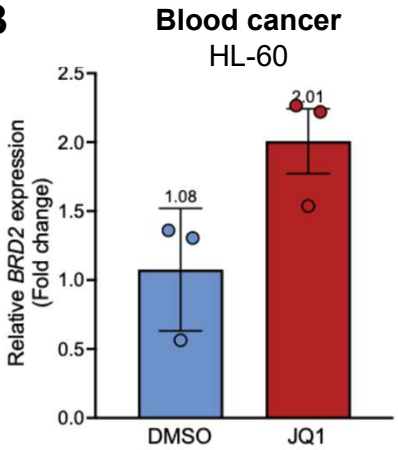

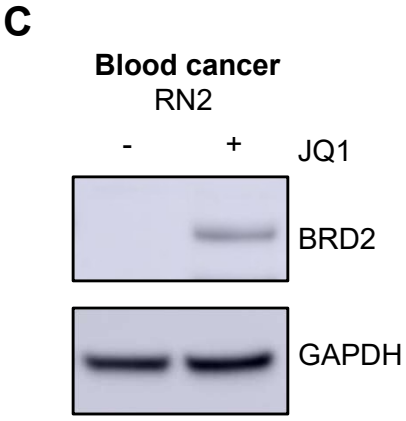

Supplementary Figure 2

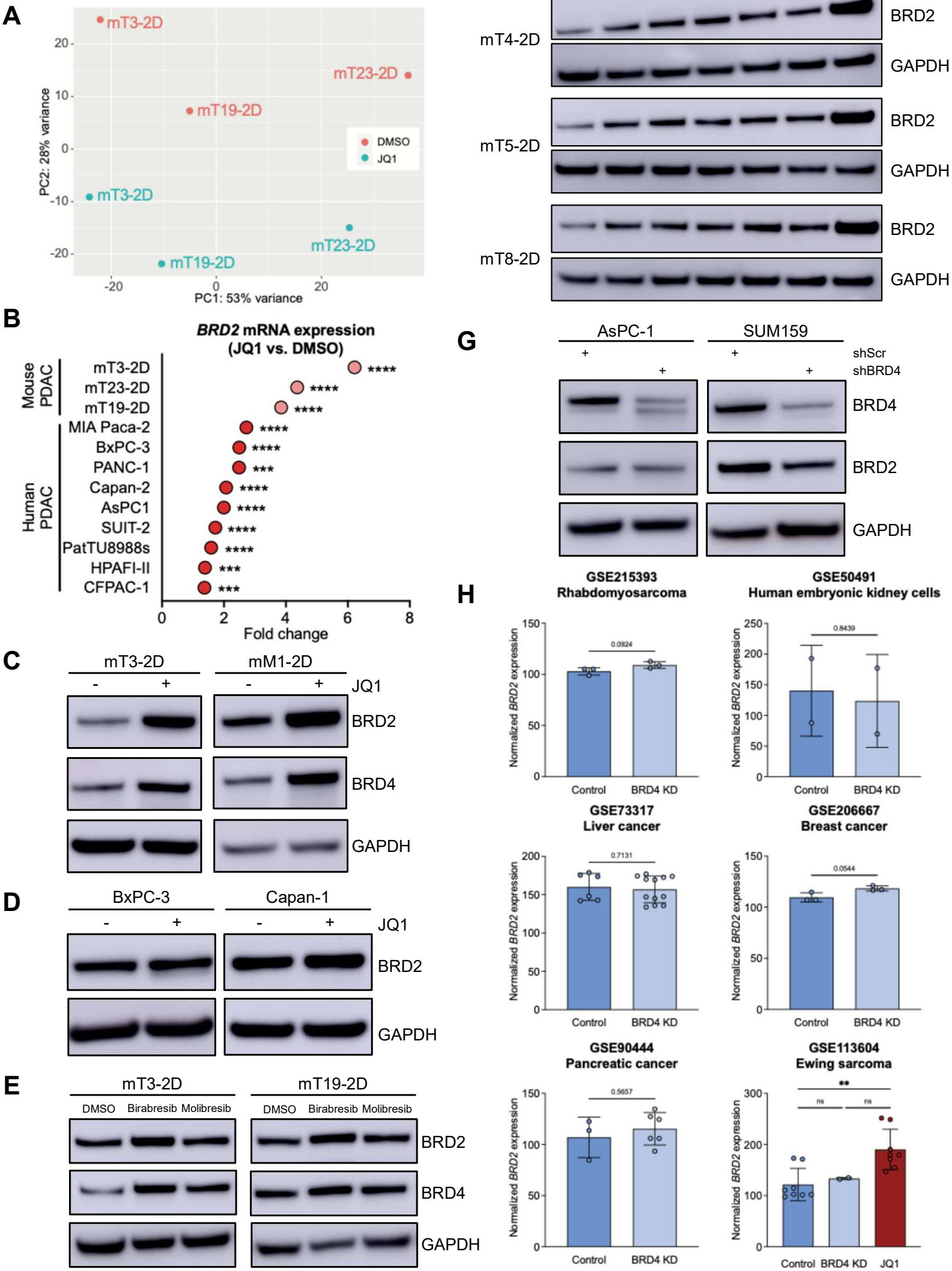

Supplementary Figure 3

A

	Gene	Function	hsa-u.4 / BRD2	hsa-r.6 / BRD2	hsa-m.7 / BRD2	hsa-m2.4 / BRD2
1	PPP1R10	protein phosphatase 1 regulatory subunit 10	8.9	8.1	5	7.7
2	NXF1	nuclear RNA export factor 1	8	6.9	2.9	7.1
3	POLR2A	RNA polymerase II subunit A	7.6	6.7	2.8	6.6
4	RBM22	RNA binding motif protein 22	7.5	7.8	2.6	5.3
5	FAM193A	family with sequence similarity 193 member A	7.4	7.4	1.1	5.6
6	BRPF3	bromodomain and PHD finger containing 3	7.1	5.5	1.7	6.9
7	PRRC2A	proline rich coiled-coil 2A	6.8	6.2	3.4	5.8
8	BTN2A1	butyrophilin subfamily 2 member A1	6.8	6.7	1.9	5.1
9	TRIM39	tripartite motif containing 39	6.7	5.9	2.8	5.9
10	SRCAP	Snf2 related CREBBP activator protein	6.6	5	1.8	6.6
11	BRPF1	bromodomain and PHD finger containing 1	6.6	6.1	1.9	5.4
12	RSRC2	arginine and serine rich coiled-coil 2	6.6	7.1	2.9	4.4
13	KDM2A	lysine demethylase 2A	6.5	6.5	2.7	4.9
14	SCAF4	SR-related CTD associated factor 4	6.2	5.8	1	5.1
15	FAM53C	family with sequence similarity 53 member C	6.2	5.4	2.1	5.6
16	CCNL1	cyclin L1	6.2	6.8	1.3	4.1
17	EP300	E1A binding protein p300	6.2	5.4	1.9	5.5
18	ABCF1	ATP binding cassette subfamily F member 1	6.2	6	2.2	4.8
19	PHF12	PHD finger protein 12	6.1	5.8	1.2	5
20	CNOT4	CCR4-NOT transcription complex subunit 4	6.1	7.5	1.5	3.2
21	TRIM26	tripartite motif containing 26	6.1	7	2.6	3.7
22	ZNF592	zinc finger protein 592	6	4.1	0.6	6.4
23	ATXN2L	ataxin 2 like	5.9	5.1	1.9	5.3
24	ZNF335	zinc finger protein 335	5.8	5.3	1.8	5
25	SETD5	SET domain containing 5	5.8	6	2.3	4.2
26	CDK12	cyclin dependent kinase 12	5.8	6	0.6	4.2
27	NUP153	nucleoporin 153	5.8	5.6	1.8	4.5
28	CREBBP	CREB binding protein	5.8	5.2	0.9	5
29	SRRM2	serine/arginine repetitive matrix 2	5.8	4	5.1	6.2
30	**NFYA**	**nuclear transcription factor Y subunit alpha**	**5.7**	**5.6**	**1.7**	**4.4**
31	YTHDC1	YTH domain containing 1	5.7	6.1	2.3	4
32	SCAF8	SR-related CTD associated factor 8	5.6	5	1.6	4.9
33	QRICH1	glutamine rich 1	5.6	5.9	0.2	4
34	PHF1	PHD finger protein 1	5.6	4	2.4	5.8
35	SF1	splicing factor 1	5.5	5	2.6	4.7
36	SUPT6H	SPT6 homolog: histone chaperone and transcription elongation factor	5.5	5.5	1.8	4.1
37	MEPCE	methylphosphate capping enzyme	5.5	4.6	1.9	5.1
38	SRRM1	serine and arginine repetitive matrix 1	5.5	6.2	3.1	3.4
39	SFSWAP	splicing factor SWAP	5.5	5.4	3.3	4.2
40	SPEN	spen family transcriptional repressor	5.5	5.2	3.2	4.4
41	FNBP4	formin binding protein 4	5.4	5.7	1.5	3.8
42	RBM39	RNA binding motif protein 39	5.4	5.5	1.4	3.9
43	SMG7	SMG7 nonsense mediated mRNA decay factor	5.4	4	2.8	5.4
44	TSPYL2	TSPY like 2	5.3	5.5	1.1	3.8
45	HEXIM1	HEXIM P-TEFb complex subunit 1	5.3	5.2	2.6	4.1
46	PRPF4B	pre-mRNA processing factor 4B	5.3	5.8	1	3.6
47	CPSF7	cleavage and polyadenylation specific factor 7	5.3	4.4	1.9	4.9
48	ARID1A	AT-rich interaction domain 1A	5.3	4.8	1.9	4.6
49	CDC5L	cell division cycle 5 like	5.3	5.5	2.2	3.8
50	PPP1R11	protein phosphatase 1 regulatory inhibitor subunit 11				

B

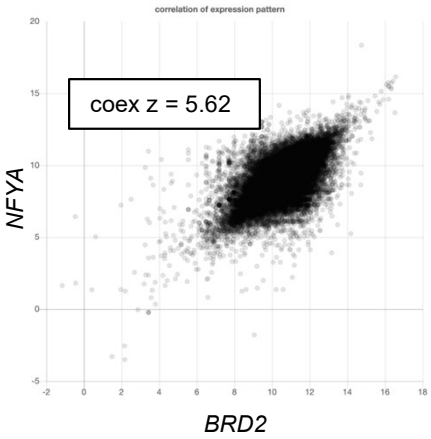

C

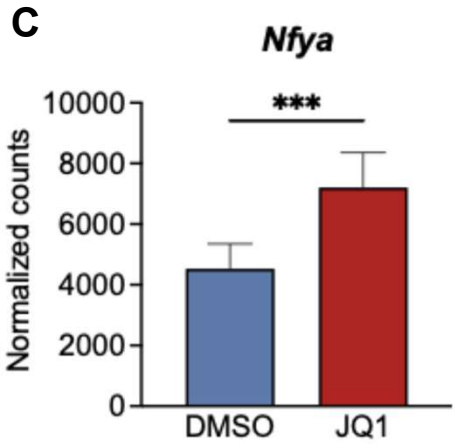

Supplementary Figure 4

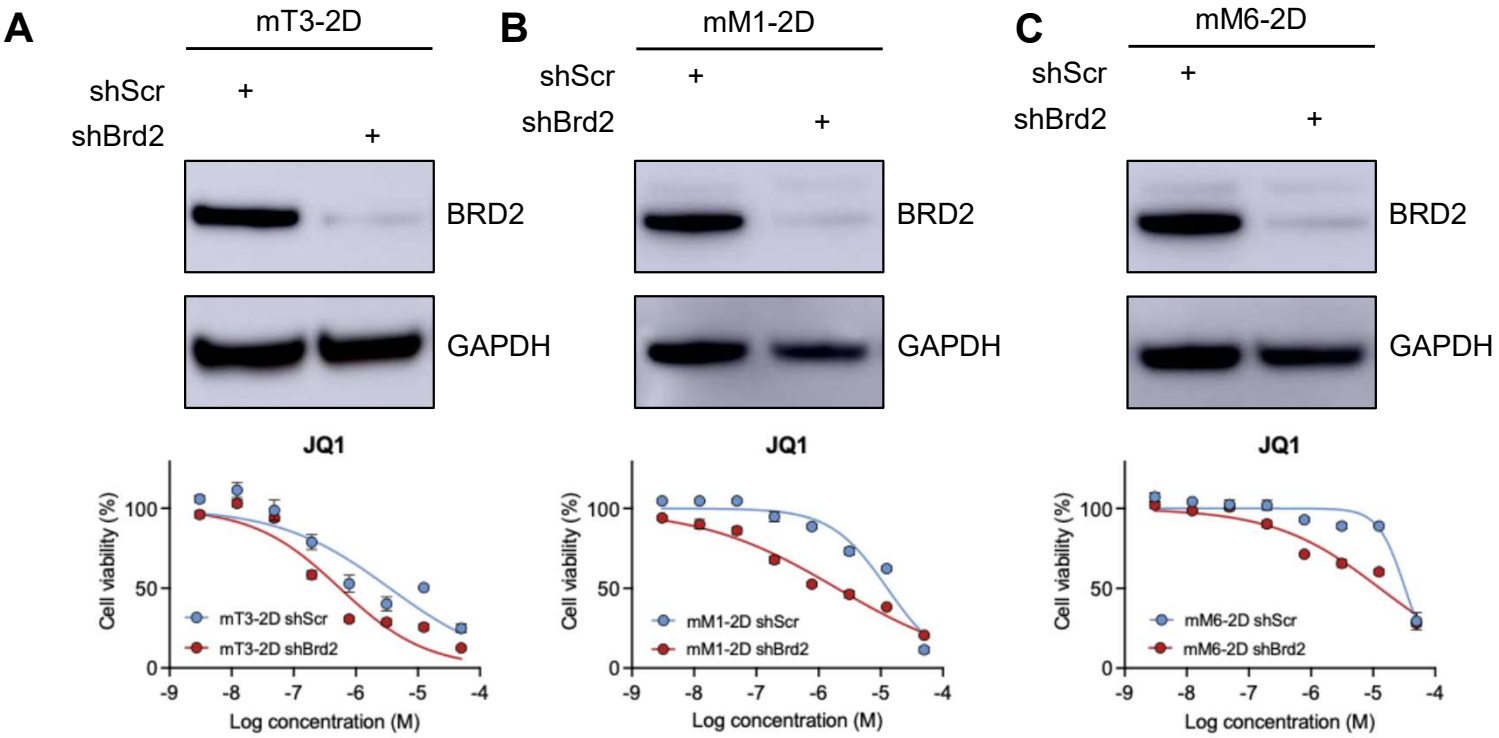

Supplementary Figure 5

A

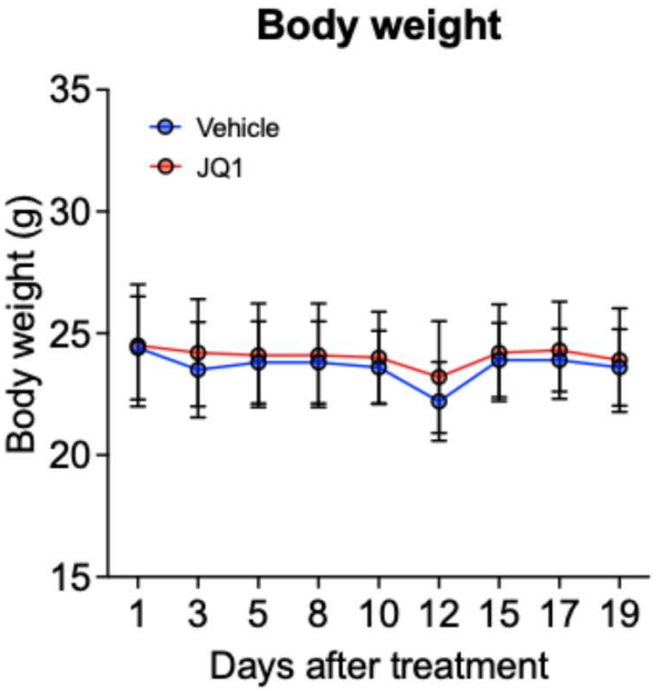
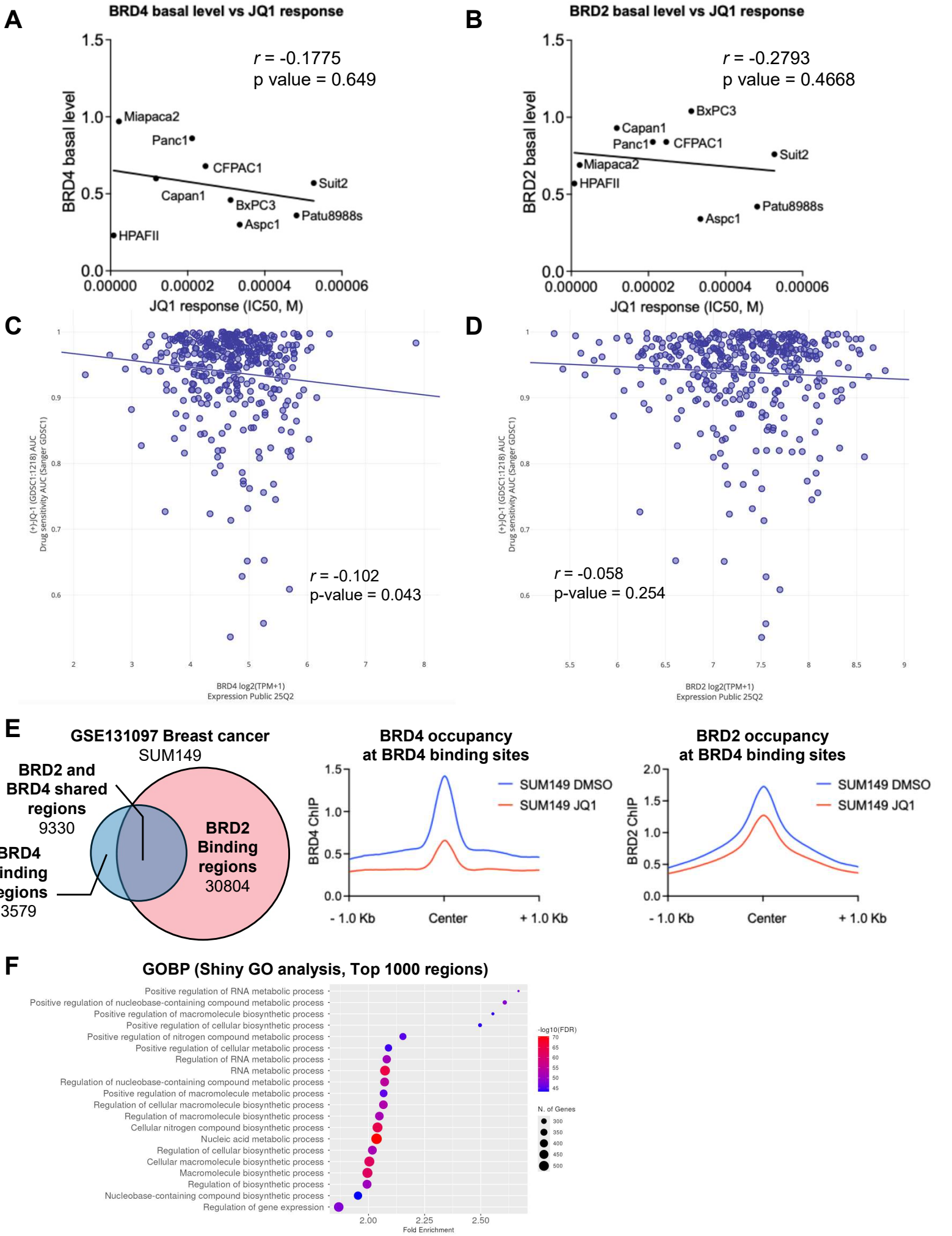
Supplementary Figure 6